

Observing structural disorder induced interacting topological phase in an atom array

Zongpei Yue,^{1,2,*} Yu-Feng Mao,^{3,*} Xinhui Liang,^{1,4,*} Zhen-Xing Hua,^{1,2} Peiyun Ge,^{1,2} Yu-Xin Chao,^{1,2} Kai Li,^{3,5} Chen Jia,^{1,2} Meng Khoon Tey,^{1,2,6,†} Yong Xu,^{3,6,‡} and Li You^{1,2,4,6,§}

¹*State Key Laboratory of Low Dimensional Quantum Physics,
Department of Physics, Tsinghua University, Beijing 100084, China*

²*Frontier Science Center for Quantum Information, Beijing, China*

³*Center for Quantum Information, IIIS, Tsinghua University, Beijing 100084, China*

⁴*Beijing Academy of Quantum Information Sciences, Beijing 100193, China*

⁵*RIKEN Center for Emergent Matter Science (CEMS), Wako, Saitama 351-0198, Japan*

⁶*Hefei National Laboratory, Hefei, Anhui 230088, China*

Topological phases of matter can appear in noninteracting systems^{1–3}, as in band topology, or interacting systems⁴, such as in spin models, with their defining features typically robust against weak disorder. Intriguingly, disorder itself can also induce topological phases—exemplified by the Anderson topological insulator in noninteracting systems⁵. Experimental studies on disorder induced topology have so far been limited to band topology^{6–14}. Here we report direct observations of structural disorder induced many-body interacting topological phase in an atom array at half-filling, whereby random offsets to tweezer locations forming a lattice implement structural disorder, causing fluctuating long-range dipolar interactions between tweezer confined single atoms. The ground state degeneracy in disordered configurations is detected and compared to a regular lattice. The induced topological phase is vindicated by the spatially resolved atom-atom correlation functions for different forms of dimer compositions. By probing the quench dynamics of a highly excited state, we observe markedly slower decay of edge spin magnetization in comparison to the bulk spin one, consistent with the presence of topologically protected edge modes in disordered lattices. Our experiments open a new direction for studying the interplay between structural disorder and strongly interacting topological matter in Rydberg atom arrays.

Topological phases of matter constitute a novel class of quantum states that extends beyond the conventional symmetry-breaking paradigm. Since disorder is ubiquitous in either natural or synthetic systems, understanding its influence on topological phases is of fundamental interest^{15,16}. Typically viewed as detrimental to ordered phase, disorder can in fact also induce topological phase—for example, in the celebrated topological Anderson insulator⁵. This counterintuitive phenomenon has motivated experimental studies across a range of systems, from the classical ones of waveguide arrays^{6,11,12}, photonic crystals^{8,13}, and acoustics^{9,10}, to the quantum ones of atomic condensates in momentum lattices⁷ and superconducting circuit¹⁴. However, all realizations are concentrated so far on noninteracting particles or fully captured by band topology of single-particle states.

Beyond band topology widely studied in single-particles or noninteracting fermions, topological phases emerge in bosonic systems as well^{4,17,18}. While free fermions settle into ground state following exclusion principle, bosons typically form a condensate as the ground state. A nontrivial symmetry-protected topological (SPT) phase can nevertheless emerge for interacting bosons in the presence of strong correlations, as cultivated by hard-core bosons, i.e., in spin-1/2 quantum models¹⁹. The classification of bosonic SPT phases involves analyzing a model's quantum many-body ground state and is systematically carried out based on group cohomology in one-dimensional (1D) systems^{20–23}. Among all SPT phases studied for interacting bosons, the Hal-

dane phase stands out as a notable example of many-body topology¹⁷ and is observed in several solid-state materials^{24,25}. In synthetic matter, an SPT phase or equivalently the Haldane state, is observed in various systems: a Rydberg atom array²⁶, a Fermi-Hubbard ladder of atoms in optical lattices²⁷, a nanographene spin chain^{28,29}, atom-based semiconductor quantum dots³⁰, and surface atoms³¹. These quantum simulations^{26–31} are implemented in lattices, either without disorder or with weak disorder. In the presence of disorder, recent studies reveal when disorder breaks the protecting symmetry, an average symmetry may exist for all possible realizations of disorder^{32–34}, giving rise to an average SPT phase³⁵. In addition, theoretical studies predict disorder can even induce a bosonic SPT phase³⁶. However, the interesting effects of disorder on interacting SPT phase remain to be observed in experiments.

This work reports the first experimental observation of a disorder induced bosonic average SPT phase. A 1D long-range SSH model for hard-core bosons (of infinite onsite interaction) is implemented with strong dipolar as well as van der Waals interactions between atoms. The initial atomic array forms a regular chain in a topologically trivial phase for either single or many particles. Structural disorder is introduced through random displacements of optical tweezers^{37–39} otherwise centered on lattice sites. At the single-particle level, edge mode emerges once disorder strength exceeds a critical threshold, confirming the structural disorder induced topological state. At near half-filling with many particles, ground

state degeneracy and correlation functions are observed, both substantiating the earlier prediction of an induced interacting topological phase³⁶. The observed quench dynamics from a highly excited state further implicate the presence of edge states by their significantly slower decay compared to atoms in the bulk. We therefore provide comprehensive evidence for the disorder induced many-body interacting topological phase, supported by measurements of the density distribution, correlation functions, microwave response, and quench dynamics.

Hard-core boson model.—Our system is described by the following 1D staggered model involving two sub-chains α and β (see Fig. 1A),

$$\hat{H} = \sum_{i < j}^{2N} J_{ij} (\hat{b}_i^\dagger \hat{b}_j + \hat{b}_j^\dagger \hat{b}_i) + \hat{H}_{\text{vdW}}, \quad (1)$$

with the vacuum and one-particle excitation states encoded into the Rydberg $|s\rangle = |0\rangle$ and $|p\rangle = \hat{b}^\dagger|0\rangle$ states, respectively⁴⁰. \hat{b}_j (\hat{b}_j^\dagger) is the annihilation (creation) operator of a boson at site j , constrained by the hard-core condition $\hat{b}_j^2 = (\hat{b}_j^\dagger)^2 = 0$. $\hat{n}_i = \hat{b}_i^\dagger \hat{b}_i$ is the particle number operator. The terms in the parentheses describe hopping from dipolar exchanges between two Rydberg atoms at sites i and j with strength given by $J_{ij} = C_3(1 - 3\cos^2\theta_{ij})/(2r_{ij}^3)$ ^{41,42} which fluctuates with the random vector \mathbf{r}_{ij} as structural disorder is introduced. C_3 is the dipolar interaction coefficient, and the external magnetic field \mathbf{B} makes an angle θ_{ij} with \mathbf{r}_{ij} . $\hat{H}_{\text{vdW}} = \sum_{i < j} V_{ij}^{\text{vdW}}(1 - \hat{n}_i)(1 - \hat{n}_j)$ denotes van der Waals interactions between Rydberg s states, with $V_{ij}^{\text{vdW}} = -C_6/r_{ij}^6$ and C_6 the corresponding coefficient. The much weaker interactions between p states are ignored. V_{ij}^{vdW} is comparable to J_{ij} in our experiment, and contributes an Ising term of the form $\sum_{i < j} \sigma_i^z \sigma_j^z$ ^{43–45}. Consequently, our model in Eq. (1) resembles the Heisenberg model with a σ^z term in the spin language⁴⁶.

The tweezers can create a regular lattice with each unit cell containing two sites separated by Δx along the direction of the chain, as shown in Fig. 1D. The atomic locations in the two sub-chains labeled α and β are denoted by $x_{2j-1} = jd$ (lattice constant d) and $x_{2j} = jd + \Delta x$ ($j = 1, 2, \dots, N$), respectively. Since the intracell hopping significantly exceeds the intercell one (e.g., 0.8 vs 0.1 MHz in our experiment), a topologically trivial phase results. Structural disorder introduces random displacements to the centers of tweezers from their regular lattice sites according to $x_{2j-1} \rightarrow x'_{2j-1} = x_{2j-1} + \delta x_j$ and $x_{2j} \rightarrow x'_{2j} = x_{2j} + \delta x_j$, i.e., each unit cell incurs a random offset δx_j along the chain, which is uniformly sampled from an interval $[-W/2, W/2]$, with W characterizing the disorder strength.

For a single atom excited into the p state, the physics can be discussed within the single-particle subspace spanned by the basis $\gamma = \{\hat{b}_1^\dagger|0\rangle, \hat{b}_2^\dagger|0\rangle, \dots, \hat{b}_{2N}^\dagger|0\rangle\}$. The corresponding Hamiltonian reduces to $[H^S]_{ij} =$

$J_{ij}(1 - \delta_{ij}) - V_i^{\text{vdW}}\delta_{ij}$ ($1 \leq i, j \leq 2N$) with $V_i^{\text{vdW}} = -C_6 \sum_{j \neq i} 1/r_{ij}^6$, apart from a constant. At the "magic angle" $\theta_m \approx 54.7^\circ$ or 125.3° , hoppings vanish along the two sub-chains, confirmed by the measured angular dependence shown in Fig. 1B. When $V_i^{\text{vdW}} = 0$, the Hamiltonian respects the sublattice symmetry, $\Pi H^S \Pi^{-1} = -H^S$, also known as chiral symmetry, with $\Pi = \text{diag}\{(-1)^j\}_{j=1}^{2N}$ the sublattice symmetry operator, leading to the \mathbb{Z} classification³. The topology of the single-particle Hamiltonian can be characterized by the polarization P_S (a topological invariant)⁴⁷, which substitutes the role played by the collective Berry phase in the regular lattice.

A nonzero V_i^{vdW} breaks the sublattice symmetry. Nevertheless, for our structural disorder model, all the Hamiltonians on random lattice configurations (\mathcal{E}_C) constitute an ensemble $\mathcal{E}_H \equiv \{H^S(C) : C \in \mathcal{E}_C\}$ respecting an average inversion symmetry with respect to x_c , which is marked by the dark blue filled circle in Fig. 1A. The average symmetry arises because the configuration $C = \{x'_j : j = 1, 2, \dots, 2N\}$ occurs with the same probability as its inversion partner $\mathcal{R}C = \{\mathcal{R}x'_j : j = 1, 2, \dots, 2N\}$, where $\mathcal{R}x'_j = 2x_c - x'_j$ is the inverted coordinate of x'_j . This allows us to generalize P_S to $P_S(C)$ for the ground states of the pair of inversion Hamiltonians $H^S(C)$ and $H^S(\mathcal{R}C)$, and prove that $P_S(C)$ is quantized to 0 or 0.5 based on the average symmetry as detailed in the Supplementary Information (SI). Since $P_S(C)$ cannot vary continuously as the Hamiltonian pair are continuously deformed, their ground states have a topological feature with $P_S(C) = 0$ for the trivial phase and $P_S(C) = 0.5$ for the nontrivial one. Accordingly, in the single-particle case, we find increasing structural disorder strength indeed induces an average SPT phase, as illustrated in Fig. 2D.

At half-filling with N atoms in the p state, we rewrite the hard-core boson model Eq. (1) as the Heisenberg model with a σ^z term, $\hat{H} = \sum_{i < j}^{2N} [(J_{ij}/2)(\sigma_i^x \sigma_j^x + \sigma_j^y \sigma_i^y) + (V_{ij}^{\text{vdW}}/4)\sigma_i^z \sigma_j^z] + (1/4) \sum_i V_i^{\text{vdW}} \sigma_i^z$. The total spin along z , $\sigma^z = \sum_i \sigma_i^z$, or the $U(1)$ symmetry, is preserved as $[\hat{H}, \sigma^z] = 0$, which confines the system to the fixed σ^z subspaces. When $V_i^{\text{vdW}} = 0$, the Hamiltonian also respects additional symmetries: rotations about x or y and time-reversal^{26,36}. In a regular lattice without disorder, the resulting SPT phase is topologically equivalent to the Haldane phase and features four-fold degenerate ground states^{26,48}. This phase is also characterized by a \mathbb{Z}_2 topological invariant P_M ⁴⁹, which is enforced by the aforementioned symmetries to be quantized for an arbitrary spin system^{36,50}. These results establish the basis for demonstrating transitions from the Affleck-Kennedy-Lieb-Tasaki (AKLT) ground state to a trivial gapped ground state⁵⁰ and an SPT phase induced by structural disorder³⁶.

A non-vanishing σ^z term breaks all the above men-

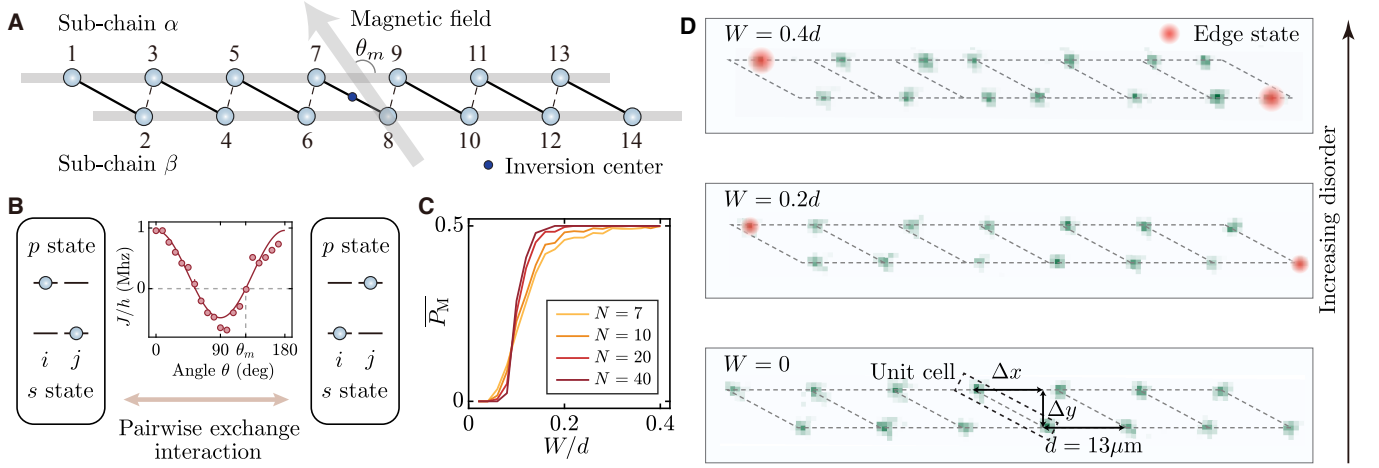


FIG. 1. Hard-core boson model with structural disorder. (A) Schematics of a dimerized 1D regular lattice with two sub-chains corresponding to a topologically trivial phase. Solid and dashed lines connecting two lattice sites represent intracell and intercell hoppings, respectively, with the line width indicating the relative strength of the hoppings. The filled dark blue circle denotes the inversion center. (B) The hopping between atoms i and j results from the dipolar exchange interaction that de-excites atom i from p to s states while simultaneously excites atom j from s to p states, or vice versa. The middle panel presents the angular (θ between \mathbf{r}_{ij} and the magnetic field \mathbf{B}) dependence of hopping strength, measured between two atoms separated by $13 \mu\text{m}$ using microwave spectroscopy, and compared to the theoretical prediction shown as a solid line. At the magic angle $\theta_m \approx 54.7^\circ$ or 125.3° , hoppings vanish along the two sub-chains. Error bars representing the standard error of the means (SEM) are smaller than the filled circle diameter. (C) Numerically calculated topological invariant \bar{P}_M (averaged over more than 150 random configurations) for our model at half-filling as a function of the structural disorder strength W , illustrating a topological phase transition from a trivial state at $\bar{P}_M = 0$ to a nontrivial phase at $\bar{P}_M = 0.5$. (D) Single-shot fluorescence images of atoms arranged into a regular lattice (outlined by the dashed lines) at $W = 0$ and disordered lattices at $W = 0.2d$ and $W = 0.4d$. As the disorder strength increases, topological edge states emerge, indicated by filled orange circles. For our experiments, $d = 13 \mu\text{m}$, $\Delta x = 0.84d$, and $\Delta y = 0.47d$; the resulting nearest-neighbor intracell hopping is about 0.8 MHz for the regular lattice, compared to a numerically estimated intercell hopping of about 0.1 MHz.

tioned symmetries except for the $U(1)$ symmetry. As a result of the average inversion symmetry mentioned before and detailed in the SI, the many-body topological invariant \bar{P}_M , analogous to the single-particle case as detailed in the SI, is generalized to $\bar{P}_M(C)$ defined as

$$\bar{P}_M(C) = \left[\frac{1}{2\pi} \text{Im} \ln \sum_{S \in \{C, \mathcal{RC}\}} \langle \Psi_S | \hat{P}_M(S) | \Psi_S \rangle \right] \bmod 1. \quad (2)$$

Here $|\Psi_S\rangle$ is the many-body ground state of the Hamiltonian \hat{H} at half-filling in the lattice configuration S under periodic boundary conditions, and $\hat{P}_M(S) = \prod_{j=1}^{2N} e^{-\frac{\pi i}{N} x_j \sigma_j^z}$ is the twist operator⁴⁹. Analogously, we prove in the SI that $\bar{P}_M(C)$ is quantized to 0 or 0.5, and thus serves as a well-defined topological invariant. Figure 1C illustrates that averaged over many independent realizations, a sharp transition with increasing structural disorder strength indeed appears, indicating that a many-body average SPT phase is induced.

Structural disorder induced topological phase at the single-particle level.—Our experiments are carried out on an array of fourteen ^{87}Rb atoms ($N = 7$)⁵¹, rather short, but comparable to earlier studies in an atom array²⁶ or quantum dots³⁰ or atoms planted on surfaces³¹.

Each atom is initially prepared in the s state (denoted by $|\uparrow\rangle \equiv |s\rangle \equiv |55S_{1/2}, m_J = -1/2\rangle$) via two-photon stimulated Raman adiabatic passage (STIRAP) from the ground state $|g\rangle \equiv |5S_{1/2}, F = 2, m_F = -2\rangle$ through the intermediate state $|e\rangle \equiv |6P_{3/2}, F = 3\rangle$. Further excitation to the p state ($|\downarrow\rangle \equiv |p\rangle \equiv |55P_{1/2}, m_J = 1/2\rangle$) is accomplished by a microwave field at a resonant frequency of about $E_0/h \sim 22.1$ GHz. A bias magnetic field of $B_z \approx 30$ G prevents cross-couplings with other magnetic sub-levels. Each experiment typically lasts for a few microseconds, during which the atomic spatial motion can be considered frozen. At the end of an experiment, atoms in the s state are de-excited to the ground state, imaged by fluorescence spectroscopy, while atoms in the p state are lost.

Using microwave spectroscopy, we determine the presence or absence of an excitation at the edge sites, thus affirmatively demonstrating the structural disorder induced topology at the single-particle level. After initializing all atoms into the s state, a weak microwave field is applied, coupling it to the p state in a process described by the Hamiltonian $\hat{H}_{\mu w} = \sum_{i=1}^{2N} [(\hbar\Omega_{\mu w}/2)(\hat{b}_i^\dagger + \hat{b}_i) - \hbar\Delta_{\mu w}\hat{b}_i^\dagger\hat{b}_i]$ with the Rabi frequency $\Omega_{\mu w}/(2\pi) \approx 0.2$ MHz and the microwave detuning $\Delta_{\mu w}$. An edge excitation will be created when the detuning matches the resonance

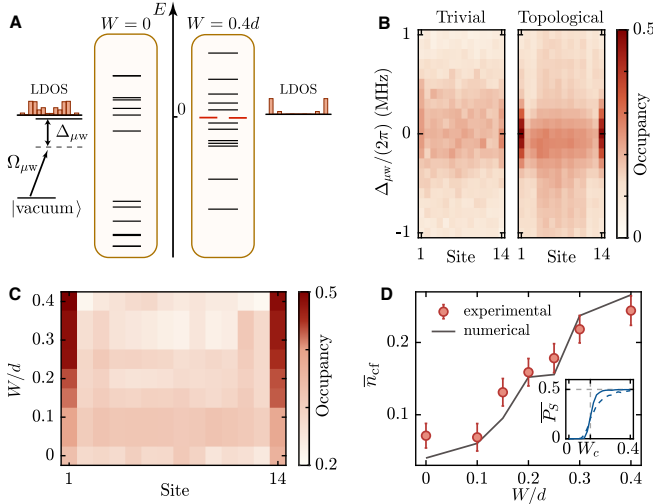


FIG. 2. **Observation of a structural disorder induced topological phase transition at the single-particle level.** (A) Single-particle spectra for regular and disordered lattices ($W = 0.4d$). In the regular lattice, no edge state near zero energy is found, while in the disordered lattice, two-fold statistically degenerate edge states emerge (dark red lines), as shown by the local density of states (LDOS). Microwaves with a Rabi frequency $\Omega_{\mu W}$ and detuning $\Delta_{\mu W}$ probe the edge states as shown in A. The energy shifts for edge states and bulk states are attributed to van der Waals interactions (see SI). (B) The dependence of measured site occupancy on the detuning $\Delta_{\mu W}$ for a regular lattice without edge states (left) and for disordered lattices with edge states at $W = 0.4d$ (right). (C) The measured dependence of site occupancy at zero detuning on structural disorder strength, showing a clear increase at two edges. (D) Contrast between the excitation of edge sites and bulk sites as a function of disorder strength from the same data in (C). The gray solid line represents the numerical result incorporating various experimental errors. Error bars are SEMs averaged over 15 random configurations. Inset: numerically computed polarization \bar{P}_s for the Hamiltonian H^S with $N = 7$ (dashed line) and $N = 40$ (solid line) as functions of disorder strength, averaged over 1000 realizations. Experimental results for disordered lattices are averaged over 15 random configurations.

as illustrated in Fig. 2A after $2.5 \mu s$. Figure 2B presents the p state occupancy in the end of excitation, revealing pronounced peaks near zero detuning at the edges of disordered lattices with $W = 0.4d$. In contrast, the same edge occupancy in the regular lattice is found to resemble closely that of the bulk. The van der Waals interactions are found to slightly modify the energy at the edges but significantly shift the bulk states, although they do not break the topological nature of the system (see SI). Our observations thus confirm the presence of edge states near zero energy in the disordered lattice as well as their absence in the regular lattice.

For further investigations, we measure the site occupancy at zero detuning as a function of disorder strength, and Fig. 2C reveals increased excitations at both edge

sites with increasing disorder strength. The phase transition is more clearly illustrated by plotting the contrast for the p state excitation n_i between edge and bulk sites, defined by $n_{cf} = (n_1 + n_{2N})/2 - \sum_{i=2}^{2N-1} n_i/(2N - 2)$. Figure 2D shows its noticeable increase with increasing disorder strength, consistent with numerical simulations that account for various experimental errors (see SI). The sharp rise around $W_c = 0.15$ provides strong evidence for a topological phase transition at the single-particle level.

Structural disorder induced topological phase for many interacting particles.—We next present results for the many-body SPT phase induced by structural disorder at half-filling. Including only nearest-neighbor hoppings and setting $\hat{H}_{vdW} = 0$, the model in Eq. (1) is mapped to a free fermion model via the inverse Jordan-Wigner transformation. Hoppings ($J_{ij} \propto r_{ij}^{-3}$) beyond the nearest neighbors, however, introduce interactions between fermions²⁶. The van der Waals interactions further give rise to Ising terms, contributing to additional fermion interactions (see SI). The experimentally realized model \hat{H} thus represents a genuine interacting many-body system. Corroborating with the sharp change in the topological invariant (Fig. 1C), the structural disorder induced bosonic average SPT phase also reveals a notable change in the many-body energy spectrum for the open boundary condition case studied. Setting $W = 0$, the spectrum features a single ground state, whereas in the disordered case with $W \neq 0$, it exhibits two statistically degenerate ground states (see Fig. 3B and 3C, and SI), which are associated with the occupation of one particle or a p state excitation at either the left or right edge, respectively. Although van der Waals interactions do not break the topology, they nevertheless introduce minor energy shifts at the edges, and cause ground states in the subspaces of $N - 1$ or $N + 1$ particles to exhibit a small energy difference (~ 0.1 MHz) to those at half-filling (more details in SI).

Many-body ground states with particle numbers near half-filling are prepared experimentally to demonstrate the induced interacting SPT phase. Atoms in an initial product state $|\psi_0\rangle$, e.g., $|1010\dots10\rangle$, $|0010\dots10\rangle$, or $|1010\dots11\rangle$, respectively in the subspaces with N , $N - 1$, and $N + 1$ particles, are arrived in steps: First, all atoms are transferred from the ground g state to the s state via STIRAP, followed by a second adiabatic protocol to the p state from a microwave pulse sweeping across the resonance; focused pinning laser beams are subsequently applied to introduce a spatially dependent AC Stark shift of $\Delta E/h \approx 20$ MHz (Fig. 3A) to the s state; finally, a second microwave pulse is swept across the resonance to produce the product state in which atoms on sites with pinning laser beams remain in the p state while getting de-excited to the s state elsewhere (Fig. 3A).

The product state $|\psi_0\rangle$ evolves into the many-body ground state following the adiabatic ramping down of the pinning laser beams (Fig. 3A), in a process described

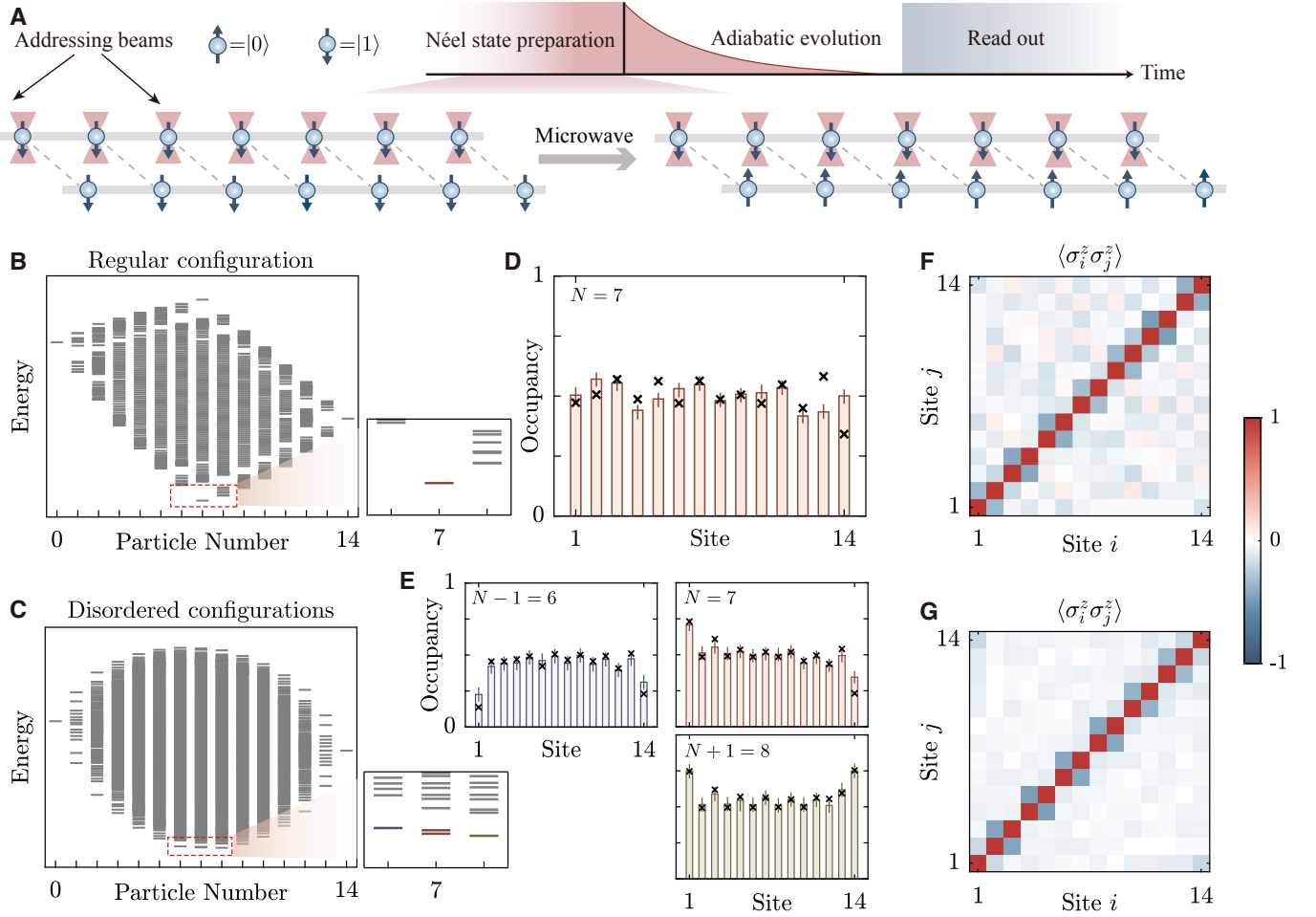


FIG. 3. Observation of structural disorder induced many-body average SPT phase. (A) Schematics of the experimental sequence for many-body ground state preparation and detection. Initially, all atoms are excited into the Rydberg p state (top left panel). Focused pinning laser beams (in a red bowtie shape) are applied to atoms in the upper sub-chain, and a microwave field is swept across resonance to produce a Néel state (right panel). Adiabatic evolution subsequently prepares the ground state of the Hamiltonian \hat{H} in a fixed particle number subspace. (B) Energy spectra at different particle numbers for a regular lattice and (C) disordered lattice ($W = 0.4d$), averaged over 15 random realizations with a zoomed-in view near the ground states. The four-fold degeneracy of the ground state is slightly lifted due to the van der Waals interactions. The average inversion symmetry only protects the two-fold ground state degeneracy in the half-filling subspace (see the SI). (D) Measured site occupancy of the ground state for the regular lattice compared to (E) the disordered lattice near half-fillings of $N-1$ (left), N (right), and $N+1$ (below) particles. The measured results are postselected for specific particle fillings. Diagonal crosses represent numerical results incorporating various experimental errors. (F) Measured two-point correlation functions of the ground state at half-filling for the regular and (G) disordered lattices, the results for the latter are averaged over 15 random configurations.

by the Hamiltonian $\hat{H}_{\text{tot}} = \hat{H} - \Delta E(t) \sum_{i \in S} \hat{n}_i$, where S denotes the set of sites with applied pinning lasers. Since this Hamiltonian respects $U(1)$ symmetry, the total particle number is conserved, and the evolving state remains within the subspace of fixed total particle number given by the initial state $|\psi_0\rangle$. At $t = 0$, the level shift is significantly larger than the energy scale of hopping terms. As a result, $|\psi_0\rangle$ is a good approximation to the ground state of \hat{H}_{tot} . After a $4 \mu\text{s}$ pulse of exponential ramping down according to $\Delta E(t) = \Delta E e^{-t/\tau}$ for $\tau = 0.6 \mu\text{s}$, we arrive at the ground state. Numerically, the above steps

achieve a fidelity better than 70% without accounting for errors (see SI).

Figures 3D and 3E present the measured occupancies for all sites of the prepared ground state in both regular and disordered lattices. While their bulk properties are comparable, their behaviors at the edge sites are significantly different. At half-filling, the edge sites in the regular lattice behave similarly to the bulk sites, whereas the disordered configuration reveals pronounced differences for either the left or right edges, as well as the imbalance between the left and right edges. In partic-

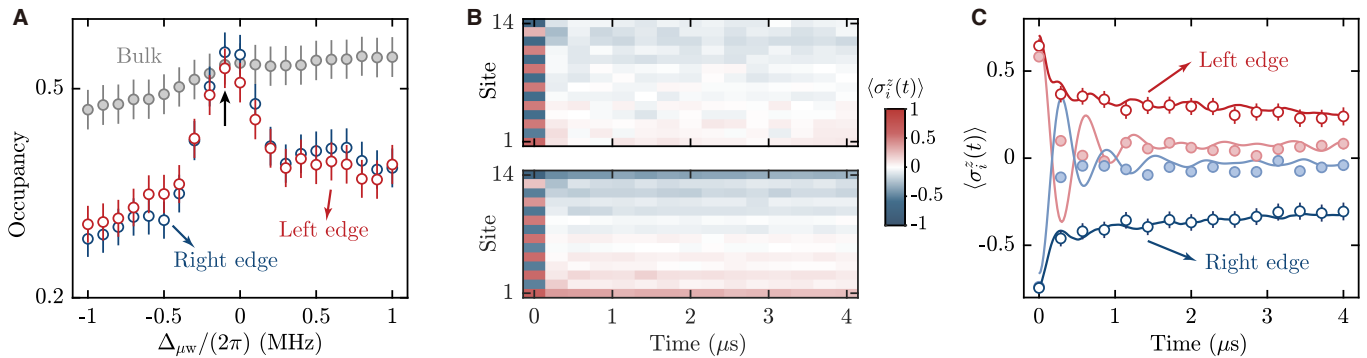


FIG. 4. **Many-body microwave spectroscopy and temporal decay of quantum spins.** (A) Measured dependence of p state occupancies for edge sites (open red and blue circles) and bulk sites (filled gray circles) on microwave detuning $\Delta_{\mu w}$ at $W = 0.4d$. A pronounced peak is observed near zero energy for both edge sites, indicating degeneracy between the two ground states at half-filling. The slight shift of the peak away from s to p resonance is due to van der Waals interactions, which lift the degeneracy between the ground states with $N - 1$ and N excitations. (B) Measured magnetization $\sigma_i^z(t)$ for all 14 sites of the initial Néel state evolved by the realized Hamiltonian in disordered lattices (lower panel) compared to the regular case (upper panel). Rapid loss of magnetization is observed for all sites except the topologically protected edge states of the disordered lattice, whose decays are significantly slower. (C) Empty circles denote results for two edge sites in (B) compared to numerical predictions incorporating various errors in solid lines at $W = 0.4d$. Filled circles correspond to the two edge states in the regular lattice. Error bars represent SEMs averaged over 15 random configurations. The experimental results for disordered lattices are averaged over 15 independent realizations.

ular, two statistically degenerate ground states exist in the half-filling subspace, one of which is presented, and is associated with a higher particle occupation at the left edge over the right one. We also observe that in the subspace with $N - 1$ particles, the occupancies of edge sites are significantly lower than in the bulk. Conversely, in the subspace with $N + 1$ particles, the edge site occupancies are notably higher. These behaviors are consistent with the expected properties of the induced topological ground states.

We further measure the correlation function $C_{i,j}^z = \langle \sigma_i^z \sigma_j^z \rangle$ for the prepared ground state at half-filling. Figures 3F and 3G reveal intracell correlations ($C_{\text{intra}}^z = \sum_{i=1}^N C_{2i-1,2i}^z / N \approx -0.38$) are significantly stronger than intercell ones ($C_{\text{inter}}^z = \sum_{i=1}^{N-1} C_{2i,2i+1}^z / (N - 1) \approx -0.15$) in the regular lattice, whereas the opposite trends are observed in the disordered lattice ($C_{\text{intra}}^z \approx -0.13$ and $C_{\text{inter}}^z \approx -0.42$). They provide smoking gun evidence that the ground state in the regular lattice is topologically trivial, while it is nontrivial in the disordered lattice.

Ground state degeneracy and quench dynamics.—We now show the observed degeneracy of the ground states in the disordered case. We first prepare a ground state with $N - 1$ particles and then employ microwave spectroscopy (as in the single-particle case) with a Rabi frequency of $\Omega_{\mu w}/(2\pi) \approx 0.25$ MHz and a pulse duration of $2 \mu s$ to probe possible excitations by scanning the detuning $\Delta_{\mu w}$. Figure 4A shows a sharp rise near zero detuning, with a distinct peak appearing at $\Delta_{\mu w}/(2\pi) \approx -0.1$ MHz for both edge sites, heralding the transition into the half-filling ground state, by adding a particle from absorption

of a resonant microwave photon to create a p state atom from an s state at the detuning of ~ -0.1 MHz for both edge sites.

Finally, we provide compelling evidence that the phase induced by structural disorder exhibits robust edge states or topological protection, even for highly excited states^{52–54}. Specifically, we initialize the system into a product state such as the Néel state $|0101 \dots 01\rangle$, a highly excited state, and subsequently evolve it under the many-body Hamiltonian \hat{H} as in a quench. In Fig. 4B, we observe that in the regular lattice, the magnetization σ_i^z for both bulk and edge sites rapidly decays to zero, implicating a quick loss of initial information or correlation. The small residual value of $\langle \sigma_i^z \rangle$ is attributed to van der Waals interactions (see SI). In contrast, in the disordered lattice, while the bulk sites exhibit a similar decay to the regular lattice, at the edges $\langle \sigma_i^z \rangle$ exhibits a slower decay and eventually stabilizes at finite values (Figs. 4B and 4C), in near complete agreement with numerical simulations.

Discussion and outlook.—Our work opens a broad avenue to study the interplay between structural disorder and topology in a fully tunable quantum platform. At the single-particle level, future explorations could address how structural disorder affects higher-dimensional topological phases, such as the Chern insulators^{55,56} and higher-order topological phases^{34,57}. At the many-body level with interactions, it is now possible to examine many-body topological phenomena in higher dimensions, including spin liquids in two-dimensional amorphous lattices^{58,59}. Furthermore, the Rydberg atom array plat-

form can be employed to explore amorphous Floquet topological phases⁶⁰ by incorporating periodic driving. In addition, it also offers new opportunities to study the interplay between localization and topology, such as topologically protected quantum dynamics in disordered systems⁵².

* These authors contributed equally to this work.

† mengkhoon_tey@tsinghua.edu.cn

‡ yongxuphy@tsinghua.edu.cn

§ lyou@mail.tsinghua.edu.cn

- [1] M. Z. Hasan and C. L. Kane, *Reviews of Modern Physics* **82**, 3045 (2010).
- [2] X.-L. Qi and S.-C. Zhang, *Reviews of Modern Physics* **83**, 1057 (2011).
- [3] C.-K. Chiu, J. C. Y. Teo, A. P. Schnyder, and S. Ryu, *Reviews of Modern Physics* **88**, 035005 (2016).
- [4] X.-G. Wen, *Reviews of Modern Physics* **89**, 041004 (2017).
- [5] J. Li, R.-L. Chu, J. K. Jain, and S.-Q. Shen, *Physical Review Letters* **102**, 136806 (2009).
- [6] S. Stützer, Y. Plotnik, Y. Lumer, P. Titum, N. H. Lindner, M. Segev, M. C. Rechtsman, and A. Szameit, *Nature* **560**, 461 (2018).
- [7] E. J. Meier, F. A. An, A. Dauphin, M. Maffei, P. Massignan, T. L. Hughes, and B. Gadway, *Science* **362**, 929 (2018).
- [8] G.-G. Liu, Y. Yang, X. Ren, H. Xue, X. Lin, Y.-H. Hu, H.-x. Sun, B. Peng, P. Zhou, Y. Chong, *et al.*, *Physical Review Letters* **125**, 133603 (2020).
- [9] F. Zangeneh-Nejad and R. Fleury, *Advanced Materials* **32**, 2001034 (2020).
- [10] H. Liu, B. Xie, H. Wang, W. Liu, Z. Li, H. Cheng, J. Tian, Z. Liu, and S. Chen, *Physical Review B* **108**, L161410 (2023).
- [11] T. Dai, A. Ma, J. Mao, Y. Ao, X. Jia, Y. Zheng, C. Zhai, Y. Yang, Z. Li, B. Tang, J. Luo, B. Zhang, X. Hu, Q. Gong, and J. Wang, *Nature Materials* **23**, 928 (2024).
- [12] X.-D. Chen, Z.-X. Gao, X. Cui, H.-C. Mo, W.-J. Chen, R.-Y. Zhang, C. T. Chan, and J.-W. Dong, *Physical Review Letters* **133**, 133802 (2024).
- [13] M. Ren, Y. Yu, B. Wu, X. Qi, Y. Wang, X. Yao, J. Ren, Z. Guo, H. Jiang, H. Chen, *et al.*, *Physical Review Letters* **132**, 066602 (2024).
- [14] X. Li, H. Xu, J. Wang, L.-Z. Tang, D.-W. Zhang, C. Yang, T. Su, C. Wang, Z. Mi, W. Sun, X. Liang, M. Chen, C. Li, Y. Zhang, K. Linghu, J. Han, W. Liu, Y. Feng, P. Liu, G. Xue, J. Zhang, Y. Jin, S.-L. Zhu, H. Yu, S. P. Zhao, and Q.-K. Xue, *Physical Review Research* **6**, L042038 (2024).
- [15] B. Kramer, T. Ohtsuki, and S. Kettemann, *Physics Reports* **417**, 211 (2005).
- [16] F. Evers and A. D. Mirlin, *Reviews of Modern Physics* **80**, 1355 (2008).
- [17] F. D. M. Haldane, *Physical Review Letters* **50**, 1153 (1983).
- [18] T. Senthil, *Annual Review of Condensed Matter Physics* **6**, 299 (2015).
- [19] S. Sachdev, *Quantum Phases of Matter* (Cambridge University Press, 2023).
- [20] X. Chen, Z.-C. Gu, and X.-G. Wen, *Physical Review B* **83**, 035107 (2011).
- [21] N. Schuch, D. Pérez-García, and I. Cirac, *Physical Review B* **84**, 165139 (2011).
- [22] F. Pollmann, A. M. Turner, E. Berg, and M. Oshikawa, *Physical Review B* **81**, 064439 (2010).
- [23] X. Chen, Z.-C. Gu, Z.-X. Liu, and X.-G. Wen, *Science* **338**, 1604 (2012).
- [24] M. Hagiwara, K. Katsumata, I. Affleck, B. I. Halperin, and J. Renard, *Physical Review Letters* **65**, 3181 (1990).
- [25] S. Glarum, S. Geschwind, K. Lee, M. Kaplan, and J. Michel, *Physical Review Letters* **67**, 1614 (1991).
- [26] S. De Léséleuc, V. Lienhard, P. Scholl, D. Barredo, S. Weber, N. Lang, H. P. Büchler, T. Lahaye, and A. Browaeys, *Science* **365**, 775 (2019).
- [27] P. Sompet, S. Hirthe, D. Bourgund, T. Chalopin, J. Bibo, J. Koepsell, P. Bojović, R. Verresen, F. Pollmann, G. Salomon, C. Gross, T. A. Hilker, and I. Bloch, *Nature* **606**, 484 (2022).
- [28] S. Mishra, G. Catarina, F. Wu, R. Ortiz, D. Jacob, K. Eimre, J. Ma, C. A. Pignedoli, X. Feng, P. Ruffieux, *et al.*, *Nature* **598**, 287 (2021).
- [29] C. Zhao, G. Catarina, J.-J. Zhang, J. C. Henriques, L. Yang, J. Ma, X. Feng, O. Gröning, P. Ruffieux, J. Fernández-Rossier, *et al.*, *Nature Nanotechnology* **19**, 1789 (2024).
- [30] M. Kiczynski, S. Gorman, H. Geng, M. Donnelly, Y. Chung, Y. He, J. Keizer, and M. Simmons, *Nature* **606**, 694 (2022).
- [31] H. Wang, P. Fan, J. Chen, L. Jiang, H.-J. Gao, J. L. Lado, and K. Yang, *Nature Nanotechnology* **19**, 1782 (2024).
- [32] L. Fu and C. L. Kane, *Physical Review Letters* **109**, 246605 (2012).
- [33] I. Fulga, B. Van Heck, J. Edge, and A. Akhmerov, *Physical Review B* **89**, 155424 (2014).
- [34] J.-H. Wang, Y.-B. Yang, N. Dai, and Y. Xu, *Physical Review Letters* **126**, 206404 (2021).
- [35] R. Ma and C. Wang, *Physical Review X* **13**, 031016 (2023).
- [36] K. Li, J.-H. Wang, Y.-B. Yang, and Y. Xu, *Physical Review Letters* **127**, 263004 (2021).
- [37] D. Barredo, S. de Léséleuc, V. Lienhard, T. Lahaye, and A. Browaeys, *Science* **354**, 1021 (2016).
- [38] M. Endres, H. Bernien, A. Keesling, H. Levine, E. R. Anschuetz, A. Krajenbrink, C. Senko, V. Vuletic, M. Greiner, and M. D. Lukin, *Science* **354**, 1024 (2016).
- [39] H. Kim, W. Lee, H.-g. Lee, H. Jo, Y. Song, and J. Ahn, *Nature Communications* **7**, 13317 (2016).
- [40] C. Chen, G. Bornet, M. Bintz, G. Emperauger, L. Leclerc, V. S. Liu, P. Scholl, D. Barredo, J. Hauschild, S. Chatterjee, M. Schuler, A. M. Läuchli, M. P. Zaletel, T. Lahaye, N. Y. Yao, and A. Browaeys, *Nature* **616**, 691 (2023).
- [41] A. Browaeys, D. Barredo, and T. Lahaye, *Journal of Physics B: Atomic, Molecular and Optical Physics* **49**, 152001 (2016).
- [42] S. Weber, C. Tresp, H. Menke, A. Urvoy, O. Firstenberg, H. P. Büchler, and S. Hofferberth, *Journal of Physics B: Atomic, Molecular and Optical Physics* **50**, 133001 (2017).
- [43] E. Urban, T. A. Johnson, T. Henage, L. Isenhower, D. D. Yavuz, T. G. Walker, and M. Saffman, *Nature Physics* **5**, 110 (2009).
- [44] G. Semeghini, H. Levine, A. Keesling, S. Ebadi, T. T.

- Wang, D. Bluvstein, R. Verresen, H. Pichler, M. Kalinowski, R. Samajdar, A. Omran, S. Sachdev, A. Vishwanath, M. Greiner, V. Vuletić, and M. D. Lukin, *Science* **374**, 1242 (2021).
- [45] S. Ebadi, A. Keesling, M. Cain, T. T. Wang, H. Levine, D. Bluvstein, G. Semeghini, A. Omran, J.-G. Liu, R. Samajdar, X.-Z. Luo, B. Nash, X. Gao, B. Barak, E. Farhi, S. Sachdev, N. Gemelke, L. Zhou, S. Choi, H. Pichler, S.-T. Wang, M. Greiner, V. Vuletić, and M. D. Lukin, *Science* **376**, 1209 (2022).
- [46] E. Manousakis, *Reviews of Modern Physics* **63**, 1 (1991).
- [47] R. Resta, *Physical Review Letters* **80**, 1800 (1998).
- [48] K. Hida, *Physical Review B* **45**, 2207 (1992).
- [49] M. Nakamura and S. Todo, *Physical Review Letters* **89**, 077204 (2002).
- [50] H. Tasaki, *Physical Review Letters* **121**, 140604 (2018).
- [51] X. Liang, Z. Yue, Y.-X. Chao, Z.-X. Hua, Y. Lin, M. K. Tey, and L. You, *Observation of anomalous information scrambling in a rydberg atom array* (2024), [arXiv:2410.16174](https://arxiv.org/abs/2410.16174) [quant-ph].
- [52] Y. Bahri, R. Vosk, E. Altman, and A. Vishwanath, *Nature communications* **6**, 7341 (2015).
- [53] X. Zhang, W. Jiang, J. Deng, K. Wang, J. Chen, P. Zhang, W. Ren, H. Dong, S. Xu, Y. Gao, F. Jin, X. Zhu, Q. Guo, H. Li, C. Song, A. V. Gorshkov, T. Iadecola, F. Liu, Z.-X. Gong, Z. Wang, D.-L. Deng, and H. Wang, *Nature* **607**, 468 (2022).
- [54] X. Mi, M. Sonner, M. Y. Niu, K. W. Lee, B. Foxen, R. Acharya, I. Aleiner, T. I. Andersen, F. Arute, K. Arya, A. Asfaw, J. Atalaya, J. C. Bardin, J. Basso, A. Bengtsson, G. Bortoli, A. Bourassa, L. Brill, M. Broughton, B. B. Buckley, D. A. Buell, B. Burkett, N. Bushnell, Z. Chen, B. Chiaro, R. Collins, P. Conner, W. Courtney, A. L. Crook, D. M. Debroy, S. Demura, A. Dunswoth, D. Eppens, C. Erickson, L. Faoro, E. Farhi, R. Fatemi, L. Flores, E. Forati, A. G. Fowler, W. Giang, C. Gidney, D. Gilboa, M. Giustina, A. G. Dau, J. A. Gross, S. Habegger, M. P. Harrigan, M. Hoffmann, S. Hong, T. Huang, A. Huff, W. J. Huggins, L. B. Ioffe, S. V. Isakov, J. Iveland, E. Jeffrey, Z. Jiang, C. Jones, D. Kafri, K. Kechedzhi, T. Khattar, S. Kim, A. Y. Kitaev, P. V. Klimov, A. R. Klotz, A. N. Korotkov, F. Kostritsa, J. M. Kreikebaum, D. Landhuis, P. Laptev, K.-M. Lau, J. Lee, L. Laws, W. Liu, A. Locharlar, O. Martin, J. R. McClean, M. McEwen, B. M. Costa, K. C. Miao, M. Mohseni, S. Montazeri, A. Morvan, E. Mount, W. Mroczkiewicz, O. Naaman, M. Neeley, C. Neill, M. Newman, T. E. O'Brien, A. Opremcak, A. Petukhov, R. Potter, C. Quintana, N. C. Rubin, N. Saei, D. Sank, K. Sankaragomathi, K. J. Satzinger, C. Schuster, M. J. Shearn, V. Shvarts, D. Strain, Y. Su, M. Szalay, G. Vidal, B. Villalonga, C. Vollgraft-Heidweiller, T. White, Z. Yao, P. Yeh, J. Yoo, A. Zalcman, Y. Zhang, N. Zhu, H. Neven, D. Bacon, J. Hilton, E. Lucero, R. Babbush, S. Boixo, A. Megrant, Y. Chen, J. Kelly, V. Smelyanskiy, D. A. Abanin, and P. Roushan, *Science* **378**, 785 (2022).
- [55] A. Agarwala and V. B. Shenoy, *Physical Review Letters* **118**, 236402 (2017).
- [56] N. P. Mitchell, L. M. Nash, D. Hexner, A. M. Turner, and W. T. Irvine, *Nature Physics* **14**, 380 (2018).
- [57] A. Agarwala, V. Jurić, and B. Roy, *Physical Review Research* **2**, 012067 (2020).
- [58] A. G. Grushin and C. Repellin, *Physical Review Letters* **130**, 186702 (2023).
- [59] G. Cassella, P. d'Ornellas, T. Hodson, W. M. Natori, and J. Knolle, *Nature Communications* **14**, 6663 (2023).
- [60] P. He, J.-X. Liu, H. Wu, and Z. D. Wang, *Floquet amorphous topological orders in a rydberg glass* (2024), [arXiv:2404.18512](https://arxiv.org/abs/2404.18512) [cond-mat].
- [61] J. Hauschild and F. Pollmann, *SciPost Phys. Lect. Notes* **5** (2018), code available from <https://github.com/tenpy/tenpy>, [arXiv:1805.00055](https://arxiv.org/abs/1805.00055).
- [62] T. L. Hughes, E. Prodan, and B. A. Bernevig, *Physical Review B* **83**, 245132 (2011).
- [63] C.-K. Chiu, H. Yao, and S. Ryu, *Physical Review B* **88**, 075142 (2013).
- [64] X. Chen, Z.-C. Gu, and X.-G. Wen, *Phys. Rev. B* **84**, 235128 (2011).
- [65] R. Thorngren and D. V. Else, *Physical Review X* **8**, 011040 (2018).
- [66] X. Chen, Z.-C. Gu, Z.-X. Liu, and X.-G. Wen, *Physical Review B* **87**, 155114 (2013).

We acknowledge significant help and enlightening discussions with Cheng Chen and Songtao Huang, and helpful contributions by Yuanjiang Tang, Chao Liang, Xiangliang Li, Xiaoling Wu, Boyang Wang, and Yifan Wang in the early stages of building up the experimental platform. We acknowledge ChatGPT for language polishing. DMRG calculations were performed using the TeNPy tensor network library⁶¹. We finally acknowledge the support by Center of High Performance Computing, Tsinghua University. This work is supported by the Innovation Program for Quantum Science and Technology (2021ZD0302100). LY is also supported by NSFC (Grants No. 12361131576 and No. 92265205). MKT is supported by NSFC (Grants. No.12234012 and W2431002). YFM, KL, and YX are supported by NSFC (Grants. No.12474265 and 11974201) and Innovation Program for Quantum Science and Technology (Grant No. 2021ZD0301604).

In the supplementary information, we provide the experimental method in Section S1, discuss experimental imperfections in Section S2, and establish the concept of the average inversion SPT phase by proving that the topological invariant is quantized by an average inversion symmetry and analyze the effects of van der Waals interactions in Section S3.

S1. EXPERIMENTAL METHOD

S1.1. Experimental platform

The realization of the model in Eq. (1) in the main text is based on a ^{87}Rb Rydberg atom array. We encode Rydberg state $|s\rangle = |55S_{1/2}\rangle$ as $|\uparrow\rangle$ and $|p\rangle = |55P_{1/2}\rangle$ as $|\downarrow\rangle$. The two pseudo-spin states are coupled by a resonant microwave at 22.1 GHz. A 30 Gauss magnetic field, aligned parallel to the plane formed by the two sub-chains, is applied to split different Zeeman states.

S1.2. Defect-free atom arrays with arbitrary configurations

In order to explore the influence of structural disorder on topological properties, we develop a rearrangement algorithm to realize arbitrary array configurations. The static tweezer array is created using an 830 nm laser modulated by a spatial light modulator (SLM). Additionally, we employ an 810 nm laser, controlled by an acousto-optic deflector (AOD) to generate a movable tweezer.

Our rearrangement strategy is based on the Hungarian algorithm, using a graph-based approach to model the entire problem. First, we prepare a tweezer array consisting of both target sites and reservoir sites. Given that the loading rate is approximately 50%, the numbers of these two types of sites are equal. The tweezers track coordinates for the nodes of a graph, while edges connect different nodes, representing the possible paths to transport atoms in our strategy. To prevent potential collisions during rearrangement, paths which are too close to other sites are not employed for rearrangement, with the threshold length set at $3.5\ \mu\text{m}$.

Once a graph is constructed, the shortest distances or paths between all pairs of nodes are computed using the Dijkstra algorithm. The lengths are stored and used as the cost for the Hungarian algorithm. The AOD is controlled by an AWG, which requires a large amount of data, therefore waveforms for transport during rearrangement along all edges are computed and stored in advance. Based on these waveforms and the associated costs, in each rearrange cycle, we determine the shortest length collection using the Hungarian algorithm and replay the stored waveforms in real time.

S1.3. Single site addressing

The initial product states are prepared with the help of an addressing laser, split from a 1013 nm laser beam and detuned from the transition between the $|\uparrow\rangle$ and an intermediate excited state $|e\rangle = |6P_{3/2}\rangle$. The addressing laser is locked to the stable 1013 nm laser employed in two-photon excitation to Rydberg states via their beat frequency, allowing for its frequency to be tuned and is set 350 MHz above the resonance.

To achieve two-dimensional single-site addressing, the addressing laser is modulated by a second SLM to generate multiple addressing beams. Each beam is focused to a radius of approximately $1.3\ \mu\text{m}$, with a typical power of 50 mW. We measure the AC Stark shift for each addressing beam by microwave spectroscopy on the $|s\rangle$ and $|p\rangle$ transition. The average AC Stark shift across the seven addressed atoms is approximately $\delta_0 \approx 2\pi \times 20\ \text{MHz}$. Daily alignment is needed to minimize atom loss and reduce AC Stark shift variations caused by mismatch between the addressing laser beams and the tweezers.

S1.4. Experimental sequence

After generating a defect-free atom array, we implement multiple cooling schemes, including polarization gradient cooling (PGC), electromagnetically induced transparency (EIT) cooling, and adiabatic ramp-down of the optical tweezers, to cool the atoms to a temperature of about $3\ \mu\text{K}$. To minimize heating effects caused by optical pumping, we first optically pump the atoms into the $|g\rangle = |5S_{1/2}, F=2, m_F=-2\rangle$ state before reducing the tweezer intensity.

Next, the magnetic field is adiabatically increased to approximately 30 Gauss. The optical tweezers are then switched off, and the atoms are excited to the Rydberg $|s\rangle$ state via two-photon stimulated Raman adiabatic passage (STIRAP) using 420 nm and 1013 nm lasers respectively coupled resonantly to the transitions $g \rightarrow e$ and $e \rightarrow s$. A microwave field at 22.1 GHz is subsequently applied to drive $|s\rangle$ and $|p\rangle$ states. Owing to the extremely large polarizability of Rydberg atoms, even a weak microwave field can induce a strong coupling. In our setup, a $-20\ \text{dBm}$ microwave field is sufficient to achieve a Rabi frequency of 2.5 MHz.

At the end of the above sequence, we measure magnetization σ_i^z at each site. Since $[\hat{H}, \sigma_i^z] \neq 0$, it is necessary to pause the interaction during readout. To achieve this, we freeze the system using a 10.38 GHz microwave pulse which excites atoms in $|p\rangle$ to the $n = 53$ hydrogenic manifold, in which atoms experience negligible interactions with those remaining in $|s\rangle$. The pulse duration is 100 ns, which is sufficiently short to minimize unwanted interactions. Subsequently, a de-excitation pulse is applied to transfer atoms in $|s\rangle$ back to the ground state using a 1013 nm laser resonantly coupling $|s\rangle$ to the short-lived intermediate $|e\rangle$ state from which atoms decay back to the ground state.

S2. EXPERIMENTAL IMPERFECTIONS

We compare the experimental results with simulations considering different imperfections in the main text. Here we discuss the main source of errors in our system, including state preparation, detection errors (SPAM), and those due to thermal motion of atoms.

S2.1. SPAM errors

As discussed earlier, atoms are transferred from $|g\rangle$ to $|s\rangle$ using STIRAP. However, a small but finite preparation error, measured to be $\eta_{\text{STIRAP}} \approx 5\% - 8\%$, results as atoms may fail to make the transition to the Rydberg state, effectively creating lattice defects. This effect is incorporated into numerical simulations by averaging over different lattice realizations.

For read out, atoms in the $|s\rangle$ state are de-excited to the ground state and subsequently recaptured in the optical tweezers. Meanwhile, atoms in the $|p\rangle$ state are repelled by the 830 nm tweezers. As a result, fluorescence detection can be used to determine which state an atom collapses into. However, atoms would be recaptured may get lost due to thermal motion over a finite evolution time, with an error probability of $\eta_e \approx 5\%$. Conversely, atoms that would be repelled by the tweezers may instead be recaptured due to the finite lifetime of Rydberg states, with a probability of $\eta_{e'} \approx 5\%$. These effects are accounted for in numerical simulations through Monte Carlo sampling.

S2.2. Errors in preparing the product state

In addition to the SPAM errors, during the preparation of the many-body ground states, errors also occur in the first step of preparing for the initial product state helped by the addressing laser. As described above, the AC Stark shift is induced by a 1013 nm laser tuned 350 MHz above the resonance between $|e\rangle$ and $|s\rangle$. However, the lifetime of the Rydberg $|s\rangle$ state, τ_s , is reduced due to coupling, albeit off resonantly to the short-lived $|e\rangle$ state

$$\tau_s \approx \left(\frac{\Delta_{\text{addr}}}{\Omega_{\text{addr}}} \right)^2 \tau_{6P}, \quad (\text{S1})$$

while the Rydberg $|p\rangle$ state remains unaffected as it is not coupled to the short lived $|e\rangle$ state by this addressing laser. To mitigate this detrimental effect of the addressing laser, we choose first to transfer all atoms into the Rydberg $|p\rangle$ state; during this process, the presence of the dipolar and van der Waals interactions gives rise to an error $\eta_{\text{MW}} \approx 0.02$. The addressing lasers are then applied to sub-chain α , inducing an AC Stark shift of approximately 20 MHz for all $|s\rangle$ state atoms in sub-chain α . Finally we sweep the MW frequency across the single-atom resonance to transfer atoms in sub-chain β to $|s\rangle$ states, with an associated error $\eta_\beta \approx 0.05$, while atoms in sub-chain α remain in $|p\rangle$ state with an error $\eta_\alpha \approx 0.04$.

S2.3. Thermal motion of atoms

Since the atoms remain at a finite temperature T , their respective velocities \mathbf{v} vary in each experimental realization, described by a Gaussian distribution with standard deviation $\Delta v = \sqrt{\frac{k_B T}{m}}$ where m is the mass of the atom. Consequently, the interaction strength fluctuates due to its dependence on both the interatomic distance and the relative angle between atoms and the magnetic field.

In a regular lattice, atoms are arranged into a configuration where intercell interactions are highly sensitive to the relative angle between the two-atom separation vector and the applied magnetic field. As a result, these interactions

exhibit greater fluctuations. In a structurally disordered lattice, thermal motion introduces an additional dependence on disorder strength. We attribute the different qualities of the correlation functions between regular and disordered lattices to this effect.

To account for thermal motion in the numerical simulations, we assume stochastic initial conditions. At the beginning of the sequence, atoms are assigned random initial positions following the above mentioned Gaussian distribution. Once the optical tweezers are switched off, atoms are given random velocities and allowed to move freely. The final results are obtained by averaging over hundreds of realizations in numerical simulations.

S3. AVERAGE SPT PHASE INDUCED BY STRUCTURAL DISORDER

In this section, we will establish the concept of the average inversion SPT phase by proving that the topological invariant is quantized by an average inversion symmetry. In addition, we will analyze the effects of van der Waals interactions. In the following, we will consider separately single-particle and many-particle cases.

S3.1. Single-particle case

In this subsection, we will focus on the Hilbert space with only a single excitation (one atom in the Rydberg p state), which is spanned by $\gamma = \{|1\rangle = \hat{b}_1^\dagger|0\rangle, |2\rangle = \hat{b}_2^\dagger|0\rangle, \dots, |2N\rangle = \hat{b}_{2N}^\dagger|0\rangle\}$. Relative to this basis, the single-particle Hamiltonian reads

$$[H^S]_{ij} = J_{ij}(1 - \delta_{ij}) - V_i^{\text{vdW}}\delta_{ij}, \quad (\text{S2})$$

which allows us to rewrite conveniently $H^S = \sum_{i,j} [H^S]_{ij} |i\rangle\langle j|$. In the following, we will prove that this Hamiltonian's topology can be characterized by the polarization (a topological invariant) protected by the average inversion symmetry.

S3.1.1. The polarization as a topological invariant

Without van der Waals interactions ($V_i^{\text{vdW}} = 0$), the single-particle Hamiltonian in Eq. (S2) respects the sublattice symmetry, i.e., $\Pi H^S \Pi^{-1} = -H^S$, with $\Pi = \text{diag}\{(-1)^j\}_{j=1}^{2N}$ the sublattice symmetry operator. Although the \mathbb{Z} classification applies for the topology protected by sublattice symmetry³, our model exhibits only two phases: a topologically trivial phase without edge modes and a nontrivial phase with one edge state at each edge. As such, we can use the polarization, which is equivalent to the Berry phase in a regular lattice, defined as⁴⁷

$$P_S = \left[\frac{1}{2\pi} \text{Im} \ln \det(U^\dagger D U) - \frac{1}{2Nd} \sum_{i=1}^{2N} x_i \right] \bmod 1, \quad (\text{S3})$$

to characterize the topology of the Hamiltonian. Here $U = (|u_1\rangle, |u_2\rangle, \dots, |u_N\rangle)$, with $|u_j\rangle$ ($j = 1, 2, \dots, N$) denoting the lowest N eigenstates of the single-particle Hamiltonian H^S under periodic boundary conditions, and $D = \text{diag}\{e^{2\pi i x_j / (Nd)}\}_{j=1}^{2N}$, with x_j the spatial coordinate of the $\lfloor (j+1)/2 \rfloor$ th unit cell. It is well known that with the sublattice symmetry, P_S can only take the values of either 0 or 0.5³⁶. This restriction allows P_S to function as a topological invariant: For a topologically trivial phase, $P_S = 0$, while for a nontrivial phase, $P_S = 0.5$.

Although the van der Waals term breaks the sublattice symmetry, our model preserves the inversion symmetry in a regular lattice and an average inversion symmetry in disordered lattices. The average symmetry enables us to generalize the polarization P_S , ensuring its quantization remains valid.

S3.1.2. Inversion symmetry

Previous studies have shown that the inversion symmetry can protect the topology in 1D^{62,63}. We now present a proof showing that, under this symmetry, the polarization P_S can only take the values of either 0 or 0.5. Specifically, consider the Hamiltonian H^S that respects the inversion symmetry, i.e., $[H^S, U_R] = 0$, where U_R is the inversion operator. When acting on $|i\rangle$, the operator yields $U_R|i\rangle = |\mathcal{R}(i)\rangle$, where $\mathcal{R}(i)$ denotes the site index of the inversion

partner of site i . This symmetry ensures that $|u_i\rangle$ in U is also an eigenstate of U_R corresponding to an eigenvalue ν_i that takes a value of 1 or -1 . With this in mind, we can derive that

$$\det(U^\dagger D U) = \det[U^\dagger U_R^\dagger (U_R D U_R^\dagger) U_R U] = \det[D_R^\dagger U^\dagger (U_R D U_R^\dagger) U D_R] = \det[U^\dagger (U_R D U_R^\dagger) U], \quad (\text{S4})$$

where we have used the fact $U_R U = U D_R$ in the derivation, with D_R an $N \times N$ diagonal matrix of the form $D_R = \text{diag}\{\nu_j\}_{j=1}^N$. Let x_c be the coordinate for the inversion center, thus $1/(2N) \sum_{i=1}^{2N} x_i = x_c$. We can also derive that

$$\begin{aligned} U_R D U_R^\dagger &= \sum_{j=1}^{2N} e^{2\pi i x_j / (Nd)} U_R |j\rangle \langle j| U_R^\dagger = \sum_{j=1}^{2N} e^{2\pi i x_j / (Nd)} |\mathcal{R}(j)\rangle \langle \mathcal{R}(j)| = \sum_{j'=1}^{2N} e^{2\pi i x_{\mathcal{R}(j')} / (Nd)} |j'\rangle \langle j'| \\ &= \sum_{j'=1}^{2N} e^{2\pi i (2x_c - x_{j'}) / (Nd)} |j'\rangle \langle j'| = e^{4\pi i x_c / (Nd)} D^\dagger. \end{aligned} \quad (\text{S5})$$

Substituting into Eq. (S4) and subsequently into Eq. (S3), then we obtain

$$P_S = \left[\frac{1}{2\pi} \text{Im} \ln \det(U^\dagger D^\dagger U) + x_c/d \right] \bmod 1. \quad (\text{S6})$$

Let $\det(U^\dagger D U) = r e^{i2\pi\theta}$ ($r > 0$). Then we obtain $P_S = (\theta - x_c/d) \bmod 1 = (-\theta + x_c/d) \bmod 1$, yielding $\theta = x_c/d + n/2$ for integer n . Therefore, $P_S = n/2 \bmod 1$ is quantized to 0 or 0.5 by the inversion symmetry.

S3.1.3. Average inversion symmetry

In the presence of structural disorder, it is clear to see that for a typical sample $C = \{x_j : j = 1, 2, \dots, 2N\}$, the Hamiltonian no longer preserves the inversion symmetry, i.e., $U_R H^S(C) U_R^{-1} \neq H^S(C)$. As a result, P_S , as defined in Eq. (S3), is not restricted to quantization at 0 or 0.5 any more, and can take other values. However, if we consider an ensemble of all possible lattice configurations, an average inversion symmetry remains. Specifically, the Hamiltonian ensemble is defined as $\mathcal{E}_H \equiv \{H^S(C) : C \in \mathcal{E}_C\}$, where \mathcal{E}_C is an ensemble containing all possible random lattice configurations. In our case, any random lattice configuration C and its inversion partner $\mathcal{R}C$ emerge in this ensemble with equal probability. As a result, the Hamiltonian $H(C)$ and its inversion conjugate partner $U_R H^S(C) U_R^{-1} = H^S(\mathcal{R}C)$ appear with the same probability. This Hamiltonian ensemble thus preserves an average inversion symmetry^{32–34}. With this observation, we identify the topological property of the Hamiltonian $H^S(C)$ and $H^S(\mathcal{R}C)$ as a whole, defining the polarization as

$$P_S(C) = \left\{ \frac{1}{2\pi} \text{Im} \ln \left[\sum_{S_0 \in \{C, \mathcal{R}C\}} e^{-i2\pi \frac{1}{2Nd} \sum_{i=1}^{2N} x_i(S_0)} \det(U(S_0)^\dagger D(S_0) U(S_0)) \right] \right\} \bmod 1, \quad (\text{S7})$$

where $D(S_0)$ and $U(S_0)$ are the corresponding matrices for the lattice configuration S_0 with coordinates of $x_i(S_0)$. Given that $H^S(C)|u_i\rangle = E_i|u_i\rangle$, we have $H^S(\mathcal{R}C)U_R|u_i\rangle = E_i U_R|u_i\rangle$, indicating that $U_R|u_i\rangle$ is the corresponding eigenstate of $H^S(\mathcal{R}C)$, or $U(\mathcal{R}C) = U_R U(C)$. Based on this, we derive that

$$\begin{aligned} U_R D(\mathcal{R}C) U_R^\dagger &= \sum_{j=1}^{2N} e^{2\pi i x_j(\mathcal{R}C) / (Nd)} U_R |j\rangle \langle j| U_R^\dagger \\ &= \sum_{j=1}^{2N} e^{2\pi i [2x_c - x_{2N+1-j}(C)] / (Nd)} |2N+1-j\rangle \langle 2N+1-j| \\ &= e^{4\pi i x_c / (Nd)} D(C)^\dagger, \end{aligned} \quad (\text{S8})$$

where $x_c = [x_j(C) + x_{2N+1-j}(\mathcal{R}C)]/2$ is the coordinate of the inversion center. We substitute Eq. (S8) into Eq. (S7), and arrive at

$$P_S(C) = \left\{ \frac{1}{2\pi} \text{Im} \ln \left[e^{-i2\pi \frac{1}{2Nd} \sum_{i=1}^{2N} x_i(C)} \det(U(C)^\dagger D(C) U(C)) + \text{c.c.} \right] \right\} \bmod 1, \quad (\text{S9})$$

indicating that $P_S(C)$ can only take the values of either 0 or 0.5.

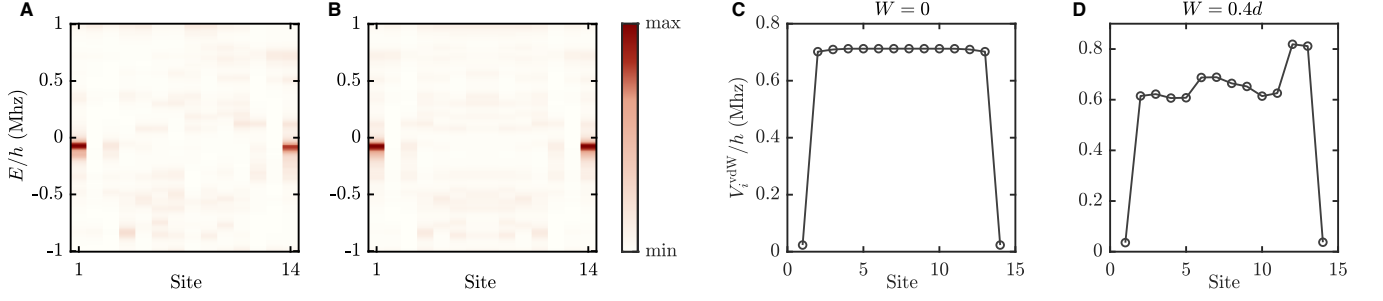


FIG. S1. Effects of van der Waals interactions. (A) and (B) Numerically calculated local density of states (DOS) for the single-particle Hamiltonian (S2) in disordered lattice ensemble with $W = 0.4d$. (C) and (D) Numerically calculated onsite energy V_i^{vdW} contributed by van der Waals interactions under open boundary conditions in a regular lattice and disordered lattices with $W = 0.4d$, respectively. In (A) and (D), the results are averaged over 15 random configurations as used in the experiments. In (B), the local DOS averaged over the experimentally used 15 configurations plus their inversion partners. We see that the local DOS is symmetric with respect to the inversion center. $C_6 = -48880 \text{ MHz} \cdot \mu\text{m}^6$ is used.

S3.1.4. Statistically degenerate edge states

Although random displacements break the inversion symmetry such that two edge states have different eigenenergies for each sample, we here will demonstrate that the two edge states remain statistically degenerate over the entire disorder ensemble.

Let $|u_L(C)\rangle$ and $|u_R(C)\rangle$ be the two edge states of the single-particle Hamiltonian $H^S(C)$ for a random configuration C under open boundary conditions. They mainly reside at the left and right edges, respectively, and their corresponding eigenenergies are $E_L(C)$ and $E_R(C)$. Due to the breaking of the inversion symmetry, $E_L(C) \neq E_R(C)$ for each realized configuration. For the inversion conjugate Hamiltonian $H^S(\mathcal{R}C)$, $|u_R(\mathcal{R}C)\rangle = U_R|u_L(C)\rangle$, and $|u_L(\mathcal{R}C)\rangle = U_R|u_R(C)\rangle$ are its eigenstates corresponding to energy $E_L(C)$ and $E_R(C)$, respectively. They are mainly localized at the right and left edges, respectively. Consider the local DOS, $\rho(i=1, E)(C)$ and $\rho(i=2N, E)(C)$ [$\rho(i=1, E)(\mathcal{R}C)$ and $\rho(i=2N, E)(\mathcal{R}C)$], at two edges at the energy E for the configuration C (the inversion partner $\mathcal{R}C$), for simplicity, we only include contributions from the edge state: At the left edge,

$$\rho(i=1, E)(C) = ||[u_L(C)]_1|^2 \delta(E - E_L(C)), \quad (\text{S10})$$

$$\rho(i=1, E)(\mathcal{R}C) = ||[u_L(\mathcal{R}C)]_1|^2 \delta(E - E_L(\mathcal{R}C)) = ||[u_R(C)]_{2N}|^2 \delta(E - E_R(C)), \quad (\text{S11})$$

and similarly for the local DOS at the right edge. For the two configurations, the average of the two local DOS at the left edge is $[\rho(i=1, E)(C) + \rho(i=1, E)(\mathcal{R}C)]/2$, which is clearly equal to the one at the right edge, $[\rho(i=2N, E)(C) + \rho(i=2N, E)(\mathcal{R}C)]/2$. Thus, it can be concluded that the two edge states are statistically degenerate. For clarity, we plot the numerically computed configuration averaged local DOS in Fig. S1B, illustrating that it preserves the inversion symmetry, and two red peaks at the left and right edges have the same energy.

S3.1.5. Effects of van der Waals interactions

In the single-particle case, van der Waals interactions contribute an onsite energy of $-V_i^{\text{vdW}}$ at site i ($i = 1, 2, \dots, 2N$). In a regular lattice with periodic boundary conditions, this onsite potential is independent of the site index. Consequently, it does not alter the eigenstates of the Hamiltonian, leaving the topology unaffected. However, under open boundary conditions as in our experiment, the potentials at edges differ from in the bulk due to the absence of one neighbor for the edge sites, as shown in Fig. S1(C). Despite this difference, the total Hamiltonian still respects the inversion symmetry, ensuring that two edge states, if they exist, are degenerate. In the figure, we see that in the bulk $V_i^{\text{vdW}}/h \approx 0.7 \text{ MHz}$, which is comparable to the intracell hopping energy of 0.77 MHz in the regular case. However, at the edges, the potential is only 0.02 MHz . This means if there were edge states in the regular lattice, we would have observed a peak of occupancy at two edges near zero detuning by microwave spectroscopy. However, our experiments (see Fig. 2(B) in the main text) do not show such a peak, implicating the absence of edge modes.

In the disordered case, for a typical configuration, V_i^{vdW} is dependent on the site index even under periodic boundary conditions. However, we have proven in the previous subsection that the topology of the ensemble of Hamiltonians

in disordered lattices can still be characterized by the generalized polarization $P_S(C)$, and edge states, if they exist, are statistically degenerate. Figure S1(D) displays the V_i^{vdW} averaged over the 15 random configurations used in experiments. We see that similarly to the regular case, V_i^{vdW} at edge sites is about 0.04 MHz. The local DOS in Figs. S1A and S1B show that the peaks at the edges appear at -0.07 MHz, whose absolute value is larger than the averaged onsite energies at the edges, possibly due to non-vanishing occupancy probabilities in the bulk sites for edge states. The existence of edge states is confirmed by our experiments, illustrating a peak of occupancy at two edges near zero detuning (see Fig. 2(B) in the main text).

S3.2. Many-particle case

In this subsection, we will focus on the case at or near half-filling (N , $N - 1$, or $N + 1$ atoms in the Rydberg p state). It is more convenient to write the Hamiltonian in Eq. (1) in the main text as a spin model

$$\hat{H} = H_{\text{XXZ}} + H_Z, \quad (\text{S12})$$

where

$$H_{\text{XXZ}} = \sum_{i < j}^{2N} \left[\frac{1}{2} J_{ij} (\sigma_i^x \sigma_j^x + \sigma_i^y \sigma_j^y) + \frac{1}{4} V_{ij}^{\text{vdW}} \sigma_i^z \sigma_j^z \right], \quad (\text{S13})$$

$$H_Z = \frac{1}{4} \sum_i V_i^{\text{vdW}} \sigma_i^z. \quad (\text{S14})$$

The Hamiltonian H_{XXZ} respects two spin-rotation symmetries along x and y respectively represented by $\hat{R}_x = \prod_{j=1}^{2N} e^{-i\pi\sigma_j^x/2}$ and $\hat{R}_y = \prod_{j=1}^{2N} e^{-i\pi\sigma_j^y/2}$, the time-reversal symmetry represented by $\hat{T} = \prod_{j=1}^{2N} \sigma_j^y \kappa$ with κ the complex conjugate operator, and a symmetry represented by $\hat{S} = \prod_{j=1}^{2N} \sigma_j^x \kappa$. The model \hat{H} preserves the total spin along z , i.e., $[\hat{H}, \sigma^z] = 0$ with $\sigma^z = \sum_i \sigma_i^z$, which corresponds to the $U(1)$ symmetry.

S3.2.1. Mapping the Hamiltonian to a fermion interacting model

We first demonstrate that the hard-core boson model in Eq. (1) in the main text or the spin model in Eq. (S12) can be mapped to a Hamiltonian of interacting fermions^{26,36} through the inverse Jordan-Wigner transformation, i.e.,

$$\hat{b}_j^\dagger = \exp(-i\pi \sum_{k=1}^{j-1} \hat{n}_k^c) \cdot \hat{c}_j^\dagger, \quad (\text{S15})$$

$$\hat{b}_j = \exp(i\pi \sum_{k=1}^{j-1} \hat{n}_k^c) \cdot \hat{c}_j. \quad (\text{S16})$$

Here, $\hat{c}_j^\dagger (\hat{c}_j)$ denotes a fermionic creation (annihilation) operator at site j , and $\hat{n}_j^c = \hat{c}_j^\dagger \hat{c}_j$ is the corresponding particle number operator. The mapped model reads

$$\hat{H}_f = \sum_{i < j}^{2N} J_{ij} \left[\hat{c}_i^\dagger e^{i\pi \sum_{k=i}^{j-1} \hat{n}_k^c} \hat{c}_j + \text{H.c.} \right] + \sum_{i < j}^{2N} V_{ij}^{\text{vdW}} (1 - \hat{n}_i^c)(1 - \hat{n}_j^c). \quad (\text{S17})$$

In addition to the interactions resulting from the long-range hoppings, the second term clearly introduces interactions between the spinless fermions. Consequently, this system exhibits genuine strong interactions.

S3.2.2. The \mathbb{Z}_2 topological invariant

To characterize the topology of the spin model Eq. (12), we define a \mathbb{Z}_2 topological invariant^{49,50}

$$P_M = \left[\frac{1}{2\pi} \text{Im} \ln \langle \Psi | \hat{\mathcal{P}}_M | \Psi \rangle \right] \bmod 1, \quad (\text{S18})$$

in analogy to the case of single particles, where $|\Psi\rangle$ is the ground state of the spin model in the symmetry sector with $\sigma^z = 0$ under periodic boundary conditions and $\hat{P}_M = \prod_{j=1}^{2N} e^{-\frac{\pi i}{Nd} x_j \sigma_j^z}$ is the twist operator with x_j denoting the position of the $\lfloor (j+1)/2 \rfloor$ th unit cell. It has been proven that any one of the above symmetries for H_{Xxz} ensures that P_M can only take the values of either 0 or 0.5³⁶, making it a well-defined topological invariant. For a topologically trivial phase, $P_M = 0$, while for a nontrivial phase, $P_M = 0.5$. Analogous to the single-particle case, van der Waals interactions introduce the H_Z term, which breaks all the above protecting symmetries. In the following, we will prove that either an inversion symmetry or an average inversion symmetry can protect the quantization of the topological invariant for the ground state in the symmetry sector with $\sigma^z = 0$.

S3.2.3. Inversion symmetry

For bosonic SPT phases, inversion symmetry plays the role of time-reversal symmetry based on the crystalline equivalence principle^{64,65}, leading to a $\mathbb{Z}_2 \times \mathbb{Z}_2$ classification in 1D⁶⁶, provided the system also respects the $U(1)$ symmetry. Here we will present a proof demonstrating that inversion symmetry can protect the quantization of P_M in the spin model. Note that an alternative proof has been provided for a spin-1 model in Ref.⁵⁰.

Specifically, suppose that the spin model has an inversion symmetry, i.e., $\mathcal{U}_R \hat{H} \mathcal{U}_R^{-1} = \hat{H}$, where \mathcal{U}_R realizes the inversion operation or $\mathcal{U}_R \sigma_j^\nu \mathcal{U}_R^{-1} = \sigma_{2N+1-j}^\nu$ ($\nu = x, y, z$). We note when the H_Z term is sufficiently large, $|\Psi\rangle$ as the ground state of this model in the symmetry sector with $\sigma^z = 0$ is no longer assured to be the global ground state of the total Hamiltonian \hat{H} . In the regular case as well as for most of the random configurations, we find that this state remains the ground state of the total Hamiltonian. In fact, ground states are prepared in a fixed symmetry sector in our experiments and we have not encountered any serious trouble with them not being that of the total Hamiltonian. In addition, we assume that $|\Psi\rangle$ is not degenerate so that $\mathcal{U}_R |\Psi\rangle = \lambda |\Psi\rangle$ with $\lambda = 1$ or -1 . We now derive that

$$\begin{aligned}
 \langle \Psi | \hat{P}_M | \Psi \rangle &= \langle \Psi | \mathcal{U}_R \hat{P}_M \mathcal{U}_R^{-1} | \Psi \rangle \\
 &= \langle \Psi | \prod_{j=1}^{2N} e^{-\frac{\pi i}{Nd} x_j \sigma_{2N+1-j}^z} | \Psi \rangle \\
 &= \langle \Psi | \prod_{j=1}^{2N} e^{-\frac{\pi i}{Nd} (2x_c - x_{2N+1-j}) \sigma_{2N+1-j}^z} | \Psi \rangle \\
 &= \langle \Psi | \hat{P}_M^\dagger | \Psi \rangle = (\langle \Psi | \hat{P}_M | \Psi \rangle)^*,
 \end{aligned} \tag{S19}$$

where we have used the fact that $\sigma^z |\Psi\rangle = 0$. This indicates that $\langle \Psi | \hat{P}_M | \Psi \rangle$ is real so that P_M has to be quantized to 0 or 0.5.

S3.2.4. Average inversion symmetry

Similar to the single-particle case, in the presence of structural disorder, for a typical configuration C , the inversion symmetry is broken, i.e., $\mathcal{U}_R \hat{H}(C) \mathcal{U}_R^{-1} \neq \hat{H}(C)$. However, the Hamiltonian ensemble $\mathcal{E}_{\hat{H}} \equiv \{\hat{H}(C) : C \in \mathcal{E}_C\}$ possesses an average inversion symmetry. In other words, the Hamiltonian $\hat{H}(C)$ and its inversion conjugate partner $\mathcal{U}_R \hat{H}(C) \mathcal{U}_R^{-1} = \hat{H}(\mathcal{R}C)$ appear with the same probability. With this average symmetry, we define a \mathbb{Z}_2 topological invariant in Eq. (2) as in the main text. We now prove that it is enforced to be quantized by the average symmetry for the ground state $|\Psi(C)\rangle$ of the configuration C and the ground state $|\Psi(\mathcal{R}C)\rangle$ of the configuration $\mathcal{R}C$ in the symmetry sector with $\sigma^z = 0$. Based on the property that $\sigma^z |\Psi(C)\rangle = 0$, we show that

$$\begin{aligned}
 \langle \Psi(\mathcal{R}C) | \hat{P}_M(\mathcal{R}C) | \Psi(\mathcal{R}C) \rangle &= \langle \Psi(C) | \mathcal{U}_R \hat{P}_M(\mathcal{R}C) \mathcal{U}_R^{-1} | \Psi(C) \rangle \\
 &= \langle \Psi(C) | \prod_{j=1}^{2N} e^{-\frac{\pi i}{Nd} x_j(\mathcal{R}C) \sigma_{2N+1-j}^z} | \Psi(C) \rangle \\
 &= \langle \Psi(C) | \prod_{j=1}^{2N} e^{-\frac{\pi i}{Nd} [2x_c - x_{2N+1-j}(C)] \sigma_{2N+1-j}^z} | \Psi(C) \rangle \\
 &= \langle \Psi(C) | \hat{P}_M(C)^\dagger | \Psi(C) \rangle = (\langle \Psi(C) | \hat{P}_M(C) | \Psi(C) \rangle)^*.
 \end{aligned} \tag{S20}$$

Thus, $\sum_{S \in \{C, \mathcal{RC}\}} \langle \Psi_S | \hat{\mathcal{P}}_M(S) | \Psi_S \rangle$ is real, and $P_M(C)$ is quantized to 0 or 0.5.

In the above proof, we have made use of the fact that σ^z is conserved corresponding to the $U(1)$ symmetry. As such, the symmetry class of the system is given by $U(1) \times (\mathbb{Z}_2^T)^{\text{avg}}$, where the spatial inversion symmetry is treated as an antiunitary \mathbb{Z}_2 internal symmetry through the crystalline equivalence principle^{64,65}. Based on previous classification results³⁵, the average SPT phase protected by $U(1) \times (\mathbb{Z}_2^T)^{\text{avg}}$ in 1D is given by

$$\sum_{p=1}^2 H^{2-p}(\mathbb{Z}_2^T, H^p(U(1), U(1))) = H^2(U(1) \times \mathbb{Z}_2^T, U(1)) / H^2(\mathbb{Z}_2^T, U(1)) = \mathbb{Z}_2, \quad (\text{S21})$$

which is consistent with the \mathbb{Z}_2 topological invariant classification.

S3.2.5. Two-fold statistically degenerate ground states at half-filling

We now show that the ground states in the subspace at half-filling with N particles in the Rydberg p state, i.e., in the subspace with $\sigma^z = 0$, are two-fold statistically degenerate under open boundary conditions for a topological phase protected by the average inversion symmetry.

Let $|\Psi_L(C)\rangle$ and $|\Psi_R(C)\rangle$ be the two ground states of the spin-model $\hat{H}(C)$ under open boundary conditions for a random configuration C with corresponding eigenenergy $E_{gL}(C)$ and $E_{gR}(C)$, respectively. These two states involve edge excitations at the left and right edges, respectively. For the inversion partner \mathcal{RC} of the configuration C , due to the fact that $\mathcal{U}_R \hat{H}(C) \mathcal{U}_R^{-1} = \hat{H}(\mathcal{RC})$, the corresponding two ground states of $\hat{H}(\mathcal{RC})$ are $|\Psi_L(\mathcal{RC})\rangle = \mathcal{U}_R |\Psi_R(C)\rangle$ and $|\Psi_R(\mathcal{RC})\rangle = \mathcal{U}_R |\Psi_L(C)\rangle$. The states $|\Psi_L(C)\rangle$ and $|\Psi_R(C)\rangle$ can be experimentally prepared by initializing into a product state $|1010\dots 10\rangle$ or $|0101\dots 01\rangle$, respectively. We are interested in the occupancy at the left edge for the state $|\Psi_L(C)\rangle$ (i.e., $\langle \Psi_L(C) | \hat{n}_1 | \Psi_L(C) \rangle$) and the occupancy at the right edge for the state $|\Psi_R(C)\rangle$ (i.e., $\langle \Psi_R(C) | \hat{n}_{2N} | \Psi_R(C) \rangle$). For a disorder ensemble \mathcal{E}_C , the average occupancy at the left and right edges are given by

$$\bar{n}_1 = \frac{1}{N_C} \sum_{C \in \mathcal{E}_C} \langle \Psi_L(C) | \hat{n}_1 | \Psi_L(C) \rangle, \quad (\text{S22})$$

and

$$\bar{n}_{2N} = \frac{1}{N_C} \sum_{C \in \mathcal{E}_C} \langle \Psi_R(C) | \hat{n}_{2N} | \Psi_R(C) \rangle, \quad (\text{S23})$$

respectively. Here N_C denotes the number of elements in the ensemble \mathcal{E}_C . To show that $\bar{n}_1 = \bar{n}_{2N}$, we only need to prove that they are equal when $\mathcal{E}_C = \{C, \mathcal{RC}\}$, thanks to the average inversion symmetry. The following derivation constitutes the proof

$$\begin{aligned} \bar{n}_1 &= \frac{1}{2} [\langle \Psi_L(C) | \hat{n}_1 | \Psi_L(C) \rangle + \langle \Psi_L(\mathcal{RC}) | \hat{n}_1 | \Psi_L(\mathcal{RC}) \rangle] \\ &= \frac{1}{2} [\langle \Psi_L(C) | \hat{n}_1 | \Psi_L(C) \rangle + \langle \Psi_R(C) | \mathcal{U}_R^{-1} \hat{n}_1 \mathcal{U}_R | \Psi_R(C) \rangle] \\ &= \frac{1}{2} [\langle \Psi_L(C) | \hat{n}_1 | \Psi_L(C) \rangle + \langle \Psi_R(C) | \hat{n}_{2N} | \Psi_R(C) \rangle] \\ &= \frac{1}{2} [\langle \Psi_R(\mathcal{RC}) | \hat{n}_{2N} | \Psi_R(\mathcal{RC}) \rangle + \langle \Psi_R(C) | \hat{n}_{2N} | \Psi_R(C) \rangle] \\ &= \bar{n}_{2N}. \end{aligned} \quad (\text{S24})$$

Thus we see the average occupancy at the two edges for the two ground states $|\Psi_L(C)\rangle$ and $|\Psi_R(C)\rangle$ over unlimited number of realizations respects the inversion symmetry. Similarly to the local DOS in the single-particle case, we can define a many-body local DOS at the left and right edges contributed by the ground states $|\Psi_L(C)\rangle$ and $|\Psi_R(C)\rangle$ as

$$\bar{\rho}(1, E) = \frac{1}{N_C} \sum_{C \in \mathcal{E}_C} \langle \Psi_L(C) | \hat{n}_1 | \Psi_L(C) \rangle \delta(E - E_{gL}(C)), \quad (\text{S25})$$

and

$$\bar{\rho}(2N, E) = \frac{1}{N_C} \sum_{C \in \mathcal{E}_C} \langle \Psi_R(C) | \hat{n}_{2N} | \Psi_R(C) \rangle \delta(E - E_{gR}(C)), \quad (\text{S26})$$

respectively. Similarly, to show that $\bar{\rho}(1, E) = \bar{\rho}(2N, E)$, we only need to prove that they are equal for $\mathcal{E}_C = \{C, \mathcal{RC}\}$. The following constitutes the proof:

$$\begin{aligned}\bar{\rho}(1, E) &= \frac{1}{2} [\langle \Psi_L(C) | \hat{n}_1 | \Psi_L(C) \rangle \delta(E - E_{gL}(C)) + \langle \Psi_L(\mathcal{RC}) | \hat{n}_1 | \Psi_L(\mathcal{RC}) \rangle \delta(E - E_{gL}(\mathcal{RC}))] \\ &= \frac{1}{2} [\langle \Psi_R(\mathcal{RC}) | \hat{n}_{2N} | \Psi_R(\mathcal{RC}) \rangle \delta(E - E_{gR}(\mathcal{RC})) + \langle \Psi_R(C) | \hat{n}_{2N} | \Psi_R(C) \rangle \delta(E - E_{gR}(C))] \\ &= \bar{\rho}(2N, E).\end{aligned}\tag{S27}$$

Thus, we conclude the two ground states $|\Psi_L(C)\rangle$ and $|\Psi_R(C)\rangle$ are two-fold statistically degenerate.

S3.2.6. Effects of van der Waals interactions

In the previous subsections, we have established the concept of the average inversion SPT phase by showing that the \mathbb{Z}_2 topological invariant is enforced to be quantized, and the ground states in the half-filling subspace is two-fold statistically degenerate.

In the following, we will show how the energy shift at the edge sites caused by van der Waals interactions lift the four-fold degeneracy. Let $|\Psi(N-1)\rangle$ and $|\Psi(N+1)\rangle$ be the ground states of H_{XXZ} in the subspace with $N-1$ and $N+1$ particles, respectively, and $|\Psi_L(N)\rangle$ and $|\Psi_R(N)\rangle$ be the two ground states of H_{XXZ} in the half-filling subspace. For H_{XXZ} , when it is topologically nontrivial, the four ground states are degenerate. However, the H_Z term modifies the spectra. For simplicity, we consider its first-order correction for a ground state $|\Psi\rangle$, i.e., $\Delta E_\Psi = \langle \Psi | H_Z | \Psi \rangle = -\frac{1}{4} \sum_{i=1}^{2N} V_i^{\text{vdW}} (2\langle \Psi | \hat{n}_i | \Psi \rangle - 1)$, where we have expressed $H_Z = -\frac{1}{4} \sum_{i=1}^{2N} V_i^{\text{vdW}} (2\hat{n}_i - 1)$ in terms of $\hat{n}_i = \hat{b}_i^\dagger \hat{b}_i$, the particle number operator at site i . For the four states involved, in the bulk sites with $2 \leq i \leq 2N-1$, we approximate $\langle \Psi | \hat{n}_i | \Psi \rangle \approx 0.5$ so that $\Delta E_\Psi \approx -\frac{1}{4} [V_1^{\text{vdW}} (2\hat{n}_1 - 1) + V_{2N}^{\text{vdW}} (2\hat{n}_{2N} - 1)]$. For $|\Psi_L(N)\rangle$ and $|\Psi_R(N)\rangle$, there is a particle occupying either the left or the right edge, respectively. We thus have $\langle \Psi_L(N) | \hat{n}_1 | \Psi_L(N) \rangle \approx 1$, $\langle \Psi_L(N) | \hat{n}_{2N} | \Psi_L(N) \rangle \approx 0$, $\langle \Psi_R(N) | \hat{n}_1 | \Psi_R(N) \rangle \approx 0$, and $\langle \Psi_R(N) | \hat{n}_{2N} | \Psi_R(N) \rangle \approx 1$. As a result, $\Delta E_{\Psi_L(N)} \approx -\frac{1}{4} (V_1^{\text{vdW}} - V_{2N}^{\text{vdW}})$ and $\Delta E_{\Psi_R(N)} = -\Delta E_{\Psi_L(N)}$. We see that for a typical realization, $\Delta E_{\Psi_L(N)} \neq \Delta E_{\Psi_R(N)}$, implying that the degeneracy is lifted. However, if we consider the inversion partner, then $\Delta E_{\Psi_L(N)}$ becomes $\frac{1}{4} (V_1^{\text{vdW}} - V_{2N}^{\text{vdW}})$ and $\Delta E_{\Psi_R(N)}$ becomes $-\frac{1}{4} (V_1^{\text{vdW}} - V_{2N}^{\text{vdW}})$. The average local DOS at the two edges remains equal at the same energy, which we have proven in the previous subsection to show that the two states are statistically degenerate. For $|\Psi(N-1)\rangle$, since no particles occupy the edges, $\langle \Psi(N-1) | \hat{n}_1 | \Psi(N-1) \rangle \approx 0$ and $\langle \Psi(N-1) | \hat{n}_{2N} | \Psi(N-1) \rangle \approx 0$. Thus, $\Delta E_{\Psi(N-1)} = \frac{1}{4} (V_1^{\text{vdW}} + V_{2N}^{\text{vdW}})$. For $|\Psi(N+1)\rangle$, there are two particles occupying the edges so that $\langle \Psi(N+1) | \hat{n}_1 | \Psi(N+1) \rangle \approx 1$ and $\langle \Psi(N+1) | \hat{n}_{2N} | \Psi(N+1) \rangle \approx 1$. Thus, $\Delta E_{\Psi(N+1)} = -\frac{1}{4} (V_1^{\text{vdW}} + V_{2N}^{\text{vdW}})$. We therefore conclude that van der Waals interactions lift the degeneracy between the two ground states $\Delta E_{\Psi(N-1)}$ and $\Delta E_{\Psi(N+1)}$, with their energy difference of about $\frac{1}{2} |V_1^{\text{vdW}} + V_{2N}^{\text{vdW}}|$.

Figure S1(D) shows that $V_1^{\text{vdW}}/h, V_{2N}^{\text{vdW}}/h \sim 0.04$ MHz, suggesting an energy difference of about 0.04 MHz. However, our numerical results show that the two ground states exhibit an energy difference of about 0.2 MHz on average. This can be probably attributed to the distribution of edge states inside the bulk sites, where energy shifts by van der Waals interactions are much larger than at the edges. The energy difference between the ground state in the subspace with $N-1$ and N particles is about 0.1 MHz, which is consistent with our experimental observation that an occupancy peak at two edges arises at the detuning of -0.1 MHz (see Fig. 4A in the main text).

S3.2.7. Adiabatic preparation of the many-body ground state

Here we present numerical analyses of the adiabatic preparation for the many-body ground state in a subspace with a fixed particle number. As stated in the main text, we first prepare a product state $|\psi_0\rangle$, such as $|1010\dots 10\rangle$, $|0010\dots 10\rangle$, or $|1010\dots 11\rangle$, which lie in the subspaces of N (half-filling), $N-1$, and $N+1$ particles, respectively. Subsequently, we evolve it by the following Hamiltonian,

$$\hat{H}_{\text{tot}} = \hat{H} - \Delta E(t) \sum_{i \in S} \hat{n}_i,\tag{S28}$$

where S represents the set of sites with applied pinning lasers. Since $\Delta E(t=0)/h = 20$ MHz is much larger than the energy scale in \hat{H} , the state $|\psi_0\rangle$ is a good approximation to the ground state of \hat{H}_{tot} . During the time evolution, we

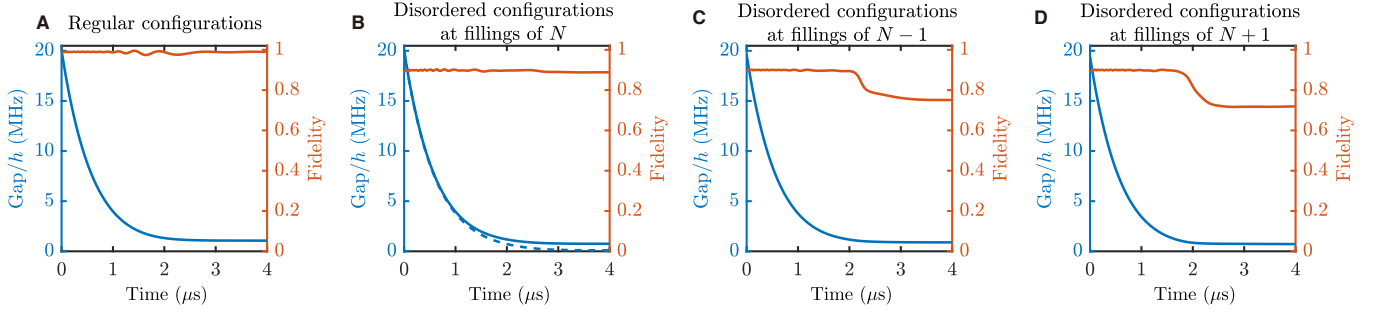


FIG. S2. Numerically calculated energy gap and state fidelity between the evolving state and the true ground state for (A) the regular configuration and (B-D) disordered configurations at varying filling numbers and averaged over 15 random configurations. In B, the solid line represents the energy gap between the third lowest energy state and the lowest energy state, while the dashed line corresponds to the gap between the second lowest energy state and the lowest energy state.

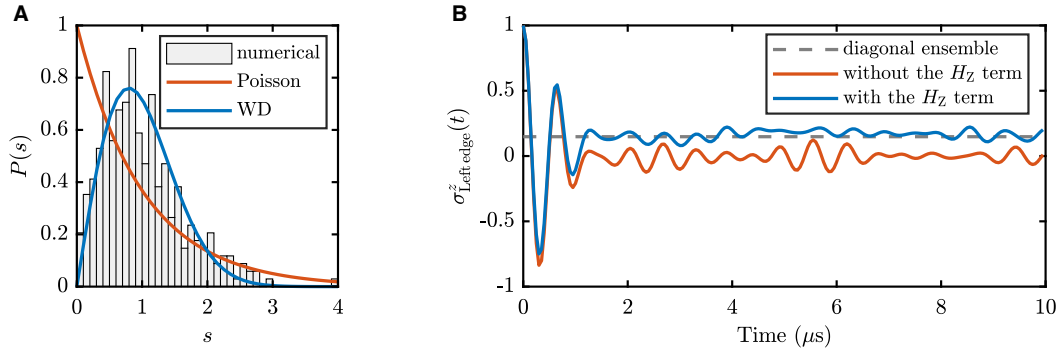


FIG. S3. The residual edge spin magnetization for the quench dynamics in the regular configuration. (A) Level-spacing statistics for the Hamiltonian in a regular lattice at half-filling with inversion symmetry resolved. The expected distributions for an integrable model (Poisson) and the corresponding chaotic or thermalized model (Wigner-Dyson) are plotted. The energy level spacing s is computed using the middle 20% of all eigenstates and rescaled such to $\langle s \rangle = 1$. (B) Magnetization from numerical simulation of quench dynamics of the left edge spin with and without the H_Z term. The dashed line represents the predicted value in the diagonal ensemble and the right edge spin shows similar long time behavior.

slowly ramp down the amplitude of the pinning lasers so that $\Delta E(t) = \Delta E e^{-t/\tau}$ with $\tau = 0.6 \mu\text{s}$. The total evolution time is $4 \mu\text{s}$.

The effectiveness of the adiabatic evolution depends on the low energy spectral gap. Figure S2 displays this gap during the time evolution. We see that for the regular configuration, the gap quickly decreases, reaching a minimum value of $\Delta_g/h = 1.06 \text{ MHz}$. For disordered configurations, the minimum energy gaps averaged over random configurations are 0.75 MHz , 0.89 MHz , and 0.72 MHz for N , $N - 1$, and $N + 1$ particles, respectively, which are slightly smaller than the minimum energy gap in the regular case. The energy gaps are on the order of the energy scale of the hopping term in the Hamiltonian \hat{H} . At half-filling, it is defined as the gap between the third lowest energy state with respect to the ground state, as the ground state is nearly two-fold degenerate. During the time evolution, although the gap declines, the ramping speed for the pinning laser beams decreases correspondingly, thereby ensuring a successful adiabatic evolution.

Figure S2 also plots the fidelity between the evolving state and the corresponding true ground state during the time evolution without accounting for errors, where the evolving state is obtained by simulating the time evolution of the Hamiltonian using the Krylov method. We see that at the end of the adiabatic evolution, the fidelity reaches 0.99 for the regular configuration. For the disordered cases, their average fidelity values are 0.89, 0.75, and 0.72 for the fillings of N , $N - 1$, and $N + 1$ particles, respectively. To ensure that imperfections of the experiments are well understood, we also perform simulations by considering all SPAM errors. The results of numerical simulations are found to be in good agreement with the experimental data, as demonstrated in Fig. 3 in the main text.

S3.2.8. Effects of van der Waals interactions on quench dynamics

In Fig. 4 of the main text, we show that there exists a small residual value of magnetization $\langle \sigma_i^z \rangle$ for the edge spins over long time in the regular case in a topologically trivial phase. Here, we will demonstrate that the small residual value results from the inhomogeneous H_Z term in Eq. (S12) introduced by van der Waals interactions. Notably, the σ^z terms are nearly zero at the edges while being finite and large in the bulk (see Fig. S1C).

Without the H_Z term, we observe that the initially polarized local spins delocalize and spread across the chain due to spin exchange processes, i.e., a particle can hop to other sites in the hard-core boson language. Over time, the spin distribution becomes homogeneous, leading to an average magnetization of $\langle \sigma_i^z \rangle = 0$ at every site (see Fig. S3B). In the presence of a homogeneous H_Z term, the physics remains unchanged since the dynamics are restricted to the subspace of $\sigma^z = 0$. This indicates that the slight residual arises from the difference in the H_Z term between the edges and the bulk. Due to this difference in onsite potential, bosons at the edges prefer to move into the bulk, with the energy decrease compensated for by Ising interactions between the particles.

In the regular lattice without disorder, we find that the energy-level spacing statistics satisfies the Wigner-Dyson distribution, as shown in Fig. S3A, indicating that a highly excited state can evolve in time to a thermal equilibrium state. Based on this fact, for an initial state $|\Psi(0)\rangle = \sum_{\alpha} c_{\alpha} |E_{\alpha}\rangle$, where $|E_{\alpha}\rangle$ is a Hamiltonian eigenstate with energy E_{α} and c_{α} is the corresponding expansion coefficient, the long-time expectation of σ_i^z for the initial state is given by the diagonal ensemble average,

$$\langle \sigma_i^z(t) \rangle_{t \rightarrow \infty} \approx \sum_{\alpha} |c_{\alpha}|^2 \langle E_{\alpha} | \sigma_i^z | E_{\alpha} \rangle. \quad (\text{S29})$$

We find that the expected value of $\langle \sigma^z \rangle$ at the edge is 0.15, closely matching the numerical simulations (see Fig. S3B).
